Photoinduced phase transition in tetrathiafulvalene-*p*-chloranil observed in femtosecond reflection spectroscopy

H. Okamoto,[1,2] Y. Ishige,[1] S. Tanaka,[1] H. Kishida,[1,3] S. Iwai,[2,4] and Y. Tokura[2,5]
[1]*Department of Advanced Materials Science, Graduate School of Frontier Sciences, University of Tokyo, 5-1-5 Kashiwanoha, Kashiwa, Chiba 277-8561, Japan*
[2]*Correlated Electron Research Center (CERC), National Institute of Advanced Industrial Science and Technology (AIST), Tsukuba, Ibaraki 305-8564, Japan*
[3]*Structural Ordering and Physical Properties Group, PRESTO, JST, Kawaguchi 332-0012, Japan*
[4]*Nanostructure and Material Property Group, PRESTO, JST, Kawaguchi 332-0012, Japan*
[5]*Department of Applied Physics, University of Tokyo, Tokyo 113-8656, Japan*
(Received 21 May 2004; published 5 October 2004)

Photoinduced transitions from ionic (*I*) to neutral (*N*) and neutral (*N*) to ionic (*I*) phases in an organic charge transfer (CT) complex, tetrathiafulvalene-*p*-chloranil (TTF-CA), were investigated by femtosecond pump-probe reflection spectroscopy. Transient reflectivity changes of the intramolecular transition band of TTF sensitive to the degree of CT between a donor molecule of TTF and an acceptor molecule of CA are measured as a function of excitation energy, excitation density, and temperature. By adopting the multilayer model for the analysis of the obtained transient reflectivity spectra, we have derived the time characteristics of amounts and spatial distributions of photoinduced *N* (*I*) states in the *I* (*N*) phase. The results reveal that the *I* to *N* (*IN*) transition induced by the resonant excitation of the CT band at 4 K is composed of three processes; (1) formation of a confined one-dimensional (1D) *N* domain, that is, a sequence of D^0A^0 pairs, just after the photoexcitation, (2) multiplication of the 1D *N* domains to the semimacroscopic *N* states up to 20 ps within the absorption depth of the excitation light, and (3) proceeding of the *IN* transition along the direction normal to the sample surface. At 77 K near the *NI* transition temperature (T_c=81 K), the size of the 1D *N* domain initially produced is enlarged and its multiplication process is strongly enhanced. When the excitation energy is increased, the initial photoproduct is changed from the confined 1D *N* domain to the positively and negatively charged *N* states. The spatial size of the latter is considerably larger than that of the former, indicating that the introduction of charge carriers makes the neighboring *I* state strongly unstable. The dynamics of the photoinduced *N* to *I* (*NI*) transition has also been investigated. The 1D *I* domains are initially produced by lights, however, they decay within 20 ps even if the density of the *I* domains is increased. The results demonstrate that there is a clear difference of the dynamics between the photoinduced *IN* and *NI* transitions. In these photoinduced transitions, three kinds of coherent oscillations with the period of ~0.6, ~50, and ~85 ps have been detected on the photoinduced reflectivity changes, which are reasonably assigned to the dynamical dimeric displacements of molecules associated with the spin-Peierls instability, the shock wave driven by the sudden volume change due to the photoinduced transitions, and the oscillation of the *NI* domain boundary. On the basis of the results, dynamical aspects of the photoinduced *IN* and *NI* transitions have been discussed in detail.

DOI: 10.1103/PhysRevB.70.165202 PACS number(s): 78.47.+p, 71.30.+h, 71.38.−k, 78.40.Me

I. INTRODUCTION

Control of phase transitions and related macroscopic properties by photoirradiation has recently attracted much attention.[1] This phenomenon is called photoinduced phase transition (PIPT), and is important not only as a subject in the fields of physics and chemistry, but also as a useful mechanism applicable to future optical switching devices. When one considers applications of these phenomena to switching devices, it is essentially important to control these physical properties by weak intensity of lights and in picosecond (ps) or subps time scale. A key strategy toward realizing such PIPTs is the exploration of one-dimensional (1D) materials.[1–6] 1D electronic (spin) systems essentially include instabilities inherent to electron-electron (e-e) and/or electron-lattice (e-l) interactions and sometimes produce characteristic phase transitions at low temperatures. Under the influence of these e-e and e-l interactions, a small density of photoexcitations will be able to stimulate instability of electronic states, and then dramatic PIPTs may be observed.

The 1D material we focus on in this paper is a mixed-stack charge-transfer (CT) complex, tetrathiafulvalene-*p*-chloranil (TTF-CA), which is one of the most typical examples showing PIPT.[2,7–11] The molecular structures of TTF and CA are presented in Fig. 1(a). This complex has 1D chains composed of donor (*D*) molecules (TTF) and acceptor (*A*) molecules (CA) stacking alternately as shown in Fig. 1(b).[12,13] In this type of mixed-stack CT complexes, overlap of π orbitals between adjacent *D* and *A* molecules is not so large and the transfer energy *t* along the 1D chains is smaller than on-site and nearest-neighbor e-e Coulomb interactions. The electronic structure of TTF-CA is, therefore, reasonably expressed by a localized electron picture as shown in Fig. 1(d), in which the highest occupied molecular orbital of do-

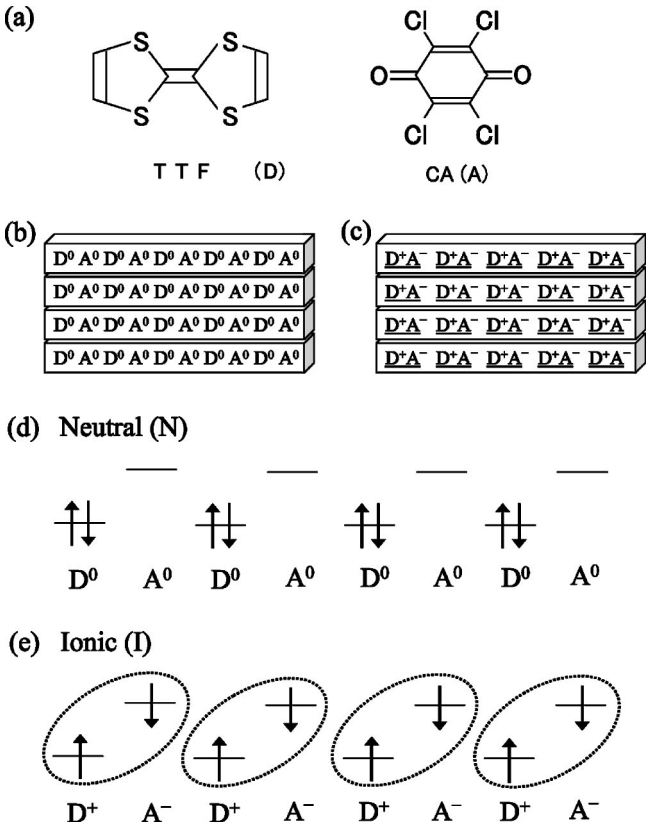

FIG. 1. Structures of TTF (donor:D) and CA (acceptor:A) molecules (a), schematic illustrations of neutral (D^0A^0) chains (b) and ionic (D^+A^-) chains (c) along the **a** axis, and the energy level structures of the neutral state (d) and ionic state (e) in TTF-CA. In the ionic phase, the D^+A^- chains are dimerized. The dimers are shown by the underlines in (c) and by the ovals in (e).

nor and the lowest unoccupied molecular orbital of acceptor are taken into account.[14] At room temperature, TTF-CA is in the neutral (N) state shown in Fig. 1(d).[14] By lowering temperature, it undergoes a neutral (N) to ionic (I) phase transition at T_c=81 K.[15–18] The effective ionization energy of TTF donor (D) and CA acceptor (A) pair is equal to I_D-E_A. Here, I_D and E_A are the ionization potential of D and the electron affinity of A, respectively. The *NI* transition is caused by the energy gain of the long range Coulomb attractive interaction overcoming the effective ionization energy of *DA* pairs.[14] The degree of CT (ρ) between TTF and CA is not equal to 0 and 1 but about 0.3 and 0.7 in the N phase and the I phase, respectively.[16,17,19] Such partial values of ρ are due to the hybridization of the N and I states through the transfer energy t. In the I phase, each molecule has essentially spin $S=1/2$ constituting the 1D spin chain, which are dimerized due to the spin-Peierls mechanism as shown in Fig. 1(e).[13,17,20–23] Therefore, the e-l interaction also plays an important role on the NI transition of TTF-CA as well as the e-e Coulomb interaction. The recent x-ray and neutron studies revealed that the directions of dimeric molecular displacements are three-dimensionally ordered in the I phase and then ferroelectric ground state is stabilized as shown in Fig. 1(c).[13,24]

In TTF-CA, thus, the neutral (N) state and the ionic (I) state are almost degenerate and the two states can be switched to each other by photoirradiations. The PIPT of TTF-CA was reported about 10 years ago by Koshihara *et al.*[2] The most striking feature of the PIPT they reported is that more than 100 *DA* pairs are changed from ionic to neutral by one photon. From the subsequent studies, they reported that the time scale of the photoinduced I to N (*IN*) transition is the order of 100 ps.[7] They also suggested that the photoinduced N to I (*NI*) transition occurs in the similar time scale as the photoinduced *IN* transition. In these studies, the excitation lights were set at 1.5–2.5 eV and polarized perpendicular to the *DA* stacking axis **a** ($\mathbf{E}\perp\mathbf{a}$), which produce the local intramolecular transition of TTF. Their energies are much higher than the peak energy of the lowest CT transition (0.65 eV). The observed dynamics of PIPT are, therefore, quite complicated and its mechanism is unclear up to the present. More recently, Suzuki *et al.* reported the behaviors of the *IN* transition induced by the irradiation of lights with the energy of 1.2 eV for $\mathbf{E}\parallel\mathbf{a}$.[8] They suggested that the relative efficiency of the photoinduced *IN* transition induced by the CT excitation is smaller than that induced by the intramolecular excitation. The used excitation energy (1.2 eV), however, corresponds to the off-resonant CT excitation with a large excess energy. To clarify the mechanism of the PIPT in TTF-CA, it will be significant to detect the dynamical behaviors of the transition under the resonant excitation of the CT band.

Here, we report the studies of the PIPT in TTF-CA using femtosecond pump-probe (p-p) reflection spectroscopy.[9,25] It has been found that the photoinduced *IN* transition is driven in picosecond time scale by the resonant excitation to the lowest CT transition, which corresponds to an excitation of neutral donor (D)-acceptor (A) (D^0A^0) pair in the ionic *DA* stacks such as $[\text{—}D^+A^-D^+A^-D^+A^-\text{—}] \rightarrow [\text{—}D^+A^-D^0A^0D^+A^-\text{—}]$. In this condition of photoexcitations, we can investigate directly the multiplication process of the D^0A^0 pairs leading to semimacroscopic photoinduced *IN* transition. To unravel the mechanism of the multiplication of D^0A^0 pairs, we have studied the excitation-density and temperature dependence of the time characteristics of the TTF intramolecular transition band, the energy of which depends sensitively on the degree of CT (ρ).[14,18,26] In the p-p reflectivity experiments, the density of absorbed photons changes depending on the distance from the sample surface and the absorption depths of the pump and probe lights are different from each other. To obtain quantitative information of the photoinduced transition from the transient reflectivity spectra, these two effects should be strictly treated. For this purpose, we adopt the multilayer model in our study. By applying this model for the analysis of the transient reflectivity spectra, the time characteristics of the amounts and spatial distributions of photoinduced products have been evaluated. The results clearly demonstrate the three-step scenario of the photoinduced *IN* transition; (1) a confined 1D N domain, that is, a sequence of D^0A^0 pairs, is initially produced from a CT excitation, (2) semimacroscopic *IN* transition occurs up to 20 ps within the absorption depth of the excitation light through the cooperative multiplication of the 1D N domains, and then (3) the *IN* transition proceeds in the direction normal to the sample surface. When the excitation

energy is increased, the dynamical behaviors of the photoinduced *IN* transition are considerably modified. The systematic studies of the p-p reflection spectroscopy reveal that the natures of the photoexcited states initially produced by the resonant CT excitation and by the higher energy excitation (or off-resonant CT excitation) are different from each other. As a result, both the dynamics and the efficiency of the *IN* transition depend strongly on the excitation energy. In this study, dynamics of the photoinduced *NI* transition has also been investigated. By the resonant excitation to the lowest CT transition expressed as $[\text{—}D^0A^0D^0A^0D^0A^0\text{—}] \rightarrow [\text{—}D^0A^0D^+A^-D^0A^0\text{—}]$, it has been found that the 1D *I* domains are initially produced in the *N* phase, however, they decay within 20 ps even if the density of the *I* domains is increased. The essential difference of the dynamics between the photoinduced *IN* and *NI* transitions will be discussed. In addition, we will report that the three kinds of coherent oscillations with the periods of ~0.6, ~50, and ~80 ps are observed in the photoinduced reflectivity changes during the photoinduced transitions. These oscillations are attributable to the dynamical dimeric displacements of molecules associated with the SP instability, the shock wave driven by the sudden volume change due to the photoinduced transition, and the oscillation of the *NI* domain boundary.

Here, we will summarize the content of this paper. In Sec. II, we detail the experimental procedures. In Sec. III, we present the polarized reflectivity spectra and the excitation profiles of the photoconductivity in both *N* and *I* phases of TTF-CA. After that, we report the results of the p-p reflection spectroscopy about the photoinduced *IN* transition and *NI* transition in Secs. IV and V, respectively. In Sec. VI, from the analysis of the obtained photoinduced reflectivity changes, we will elucidate the dynamical aspects of PIPTs, the origin of the observed coherent oscillations, and the difference between the photoinduced *IN* and *NI* transitions. The summary of this paper is given in Sec. VII.

II. EXPERIMENTAL PROCEDURES

Single crystals of TTF-CA were grown by the cosublimation of the component powder materials, which were purified by recrystallization and sublimation procedures. A typical size of the obtained crystal is $1\times0.5\times0.3$ mm^3. To perform the low temperature measurements, we used a cryostat (Oxford Optistat), in which samples are placed in cold He gas.

To probe the photoinduced *IN* and *NI* transitions, we adopted femtosecond (fs) pump-probe reflection spectroscopy. In the measurement, a Ti:sapphire (Al_2O_3) regenerative amplifier system operating at 1 kHz was employed as a light source. Output from the amplifier (800 nm:1.55 eV) with the pulse width of 130 fs was divided into two beams, which are used for the excitations of two optical parametric amplifier (OPA) systems. From the two OPA systems, the probe light pulses ranging from 1.8 to 2.6 eV and the pump light pulses ranging from 0.6 to 1.0 eV are obtained. When the pump light is set at 1.55 eV (800 nm), the output from the regenerative amplifier system itself is used. We can adjust the delay time t_d of the probe pulse relative to the pump pulse by changing the length of the route of the probe pulse.

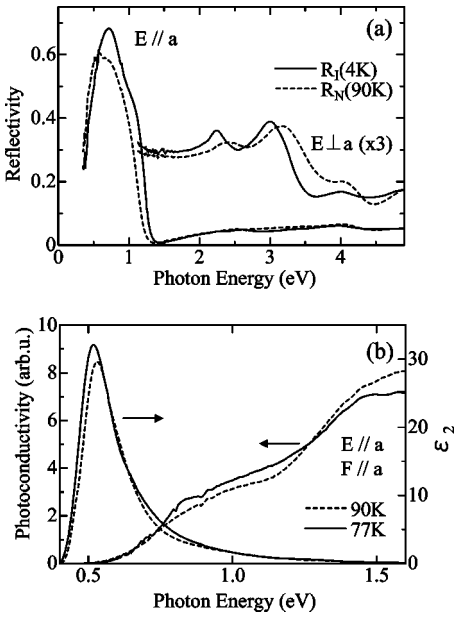

FIG. 2. (a) Polarized reflectivity spectra for the electric field of light $\mathbf{E}\|\mathbf{a}$ and $\mathbf{E}\perp\mathbf{a}$ of TTF-CA crystal on (001) surface at 4 K (solid lines: R_I) and at 90 K (broken lines: R_N). (b) Spectra of the imaginary part of dielectric constant ϵ_2 and excitation profiles of the photoconductivity at 77 K (solid line) and 90 K (broken line) for $\mathbf{E}\|\mathbf{a}$ and the applied electric field $\mathbf{F}\|\mathbf{a}$.

The time resolution of the apparatus is about 200 fs.

In the measurements of photoconductivity excitation profiles, light from a xenon lamp or a halogen-tungsten lamp was monochromized through a grating monochromator (JASCO CT-10). The monochromized light was polarized by a Glan-Taylor prism and focused on the surface of the sample. Two electrodes were put on the sides of a single crystal sample. The applied dc electric field **F** and the polarization of the excitation light **E** were set parallel (||) to the *DA* stacking axis (the **a** axis). The photocurrent, which is modulated by the incident light chopped with the frequency *f* (~270 Hz), is detected by a lock-in amplifier. The spectral intensity of the irradiated lights was corrected by using a thermopile. The thickness of the sample is much larger than the absorption depths of the incident lights. Therefore, we can consider that all the incident photons were absorbed in the sample. The excitation profile of the photoconductivity was normalized to the incident photon number by taking account of the reflection loss of the incident light. In the measurements, we have confirmed that the chopping frequency *f* (~270 Hz) of the incident light is high enough that the contributions of thermal effects are negligible compared to photogenerated ones. Linearity of the photocurrent against the applied voltage and the intensity of the incident light was also carefully checked.

III. POLARIZED REFLECTIVITY SPECTRA AND EXCITATION PROFILES OF PHOTOCONDUCTIVITY

In Fig. 2(a), we present polarized reflectivity spectra for the electric field of lights **E** parallel to the *DA* stacking axis

a (**E**∥**a**) and perpendicular to **a** (**E** ⊥ **a**) of TTF-CA crystal on the (001) plane measured at 4 K (*I* phase) and at 90 K (*N* phase). The obtained spectra are almost in agreement with those reported previously.[18,26,27] The prominent peak structures around 0.65 eV observed for **E**∥**a** in both *I* and *N* phases are due to the CT transition. The three structures at 2–4.5 eV observed for **E** ⊥ **a** are attributable to the intramolecular transition of TTF. It has been well established that these bands shift sensitively depending on ρ. In our study, we focus on the band at 2–2.5 eV. Its peak energy is 2.25 eV in the *I* phase with $\rho \sim 0.7$ and 2.4 eV in the *N* phase with $\rho \sim 0.3$.[14,18,26] Therefore, this band is a good probe of the photoinduced changes of the molecular ionicity. By measuring photoinduced reflectivity changes of this band, photoconversion of *I* (*N*) state to *N* (*I*) state can be detected.[2]

To discuss the mechanism of the *IN* or *NI* transition induced by the resonant CT excitation, it is necessary to consider nature of the CT excited state. One of the most fundamental features is whether excitonic effect is important or not. As for this, we can obtain valuable information from the excitation profiles of photoconductivity along the *DA* stack. Excitation profiles of the photoconductivity at 77 and 90 K for the electric field of light **E**∥**a** and the applied electric field **F**∥**a** are presented in Fig. 2(b) together with the imaginary part of the dielectric constant ϵ_2 spectra, which were calculated from the polarized reflectivity spectra by using the Kramers-Kronig (KK) transformation. In our experimental condition, the intensity of the incident light is extremely low, since the excitation lights are obtained by monochromizing the halogen-tungsten lamp. Therefore, we can consider that the photoinduced transition to semimacroscopic *N* state never occurs. As seen in Fig. 2(b), the photoconductivity is very small at the peak energy of the CT band in both the *I* and *N* phases, indicating that charged species are not generated by the resonant CT excitations. Namely, the excitonic effect is important in the CT excited state. The photoconductivity then gradually increases with increase of the excitation energy and, therefore, photocarriers are generated from the higher-energy excitations. As reported in the following sections, the dynamics of the photoinduced transitions in TTF-CA are strongly dependent on the excitation energy and related with whether the initial excited states are excitonic states or charged species.

IV. PHOTOINDUCED *I* TO *N* TRANSITION

A. Photoinduced *IN* transition by the resonant CT excitation

In this subsection, we present the results of the p-p reflection spectroscopy of the photoinduced *I* to *N* transition induced by the resonant CT excitation. Figure 3(a) shows the transient differential reflectivity ($\Delta R/R$) spectra of the intramolecular transition of TTF for **E** ⊥ **a** (4 K) induced by the excitation of the CT band (0.65 eV) for **E**∥**a**. Excitation (pump) density (photon number per unit area N_{ex}) is 1.2×10^{16} photons/cm^2. Taking account of the reflection loss ($\sim$68%) of the pump light and the number of photons absorbed within the absorption depth $l_p \sim 400$ Å, the average excitation density within the absorption depth l_p is estimated

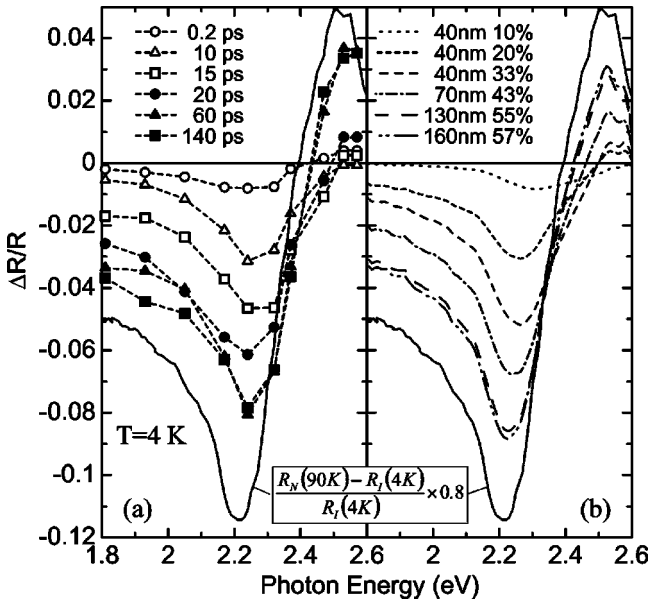

FIG. 3. (a) Transient differential reflection spectra ($\Delta R/R$) in the intramolecular transition region measured with **E** ⊥ **a** at 4 K for various time delays. The energy of the pump light (**E**∥**a**) is set to be 0.65 eV (the resonant CT excitation). Excitation density is 1.2×10^{16} photons/cm^2. The solid line shows the differential spectrum $[R_N(90\text{ K}) - R_I(4\text{ K})]/R_I(4\text{ K})$, in which $R_N(90\text{ K})$ and $R_I(4\text{ K})$ are the reflectivity spectra of the *N* phase at 90 K and the *I* phase at 4 K, respectively. (b) The differential reflection spectra ($\Delta R/R$) calculated by using the multilayer model. The used parameters β^{-1} (nm) and x_0 (%) are listed in the figure.

to be 0.24 photon/*DA* pair. Here, l_p (or equivalently the absorption coefficient $\alpha_p = 1/l_p$) was obtained from the polarized reflectivity spectrum by using the KK transformation.

The magnitudes of the spectral changes increase with the delay time t_d up to 40 ps and then almost saturate. The differential reflectivity spectrum $\{[R_N(90\text{ K}) - R_I(4\text{ K})]/R_I(4\text{ K})\}$ calculated from the reflectivity spectra in the *I* phase at 4 K, $R_I(4\text{ K})$, and in the *N* phase at 90 K, $R_N(90\text{ K})$, is shown by the solid line in the same figure. The spectral shape at $t_d = 60$ and 140 ps are almost equal to that of the calculated differential spectrum. It indicates that the *N* states are photogenerated in the *I* stacks. In the time region up to $t_d = 20$ ps, the spectral shape of $\Delta R/R$ is somewhat different from the calculated one. For example, $|\Delta R/R|$ at the high-energy region around 2.5 eV relative to $|\Delta R/R|$ at 2.25 eV $|[\Delta R/R(2.5\text{ eV})]/[\Delta R/R(2.25\text{ eV})]|$ for $t_d = 20$ ps is very small as compared with that for $t_d > 60$ ps and $[R_N(90\text{ K}) - R_I(4\text{ K})]/R_I(4\text{ K})$. Such a difference is attributable to the fact that the amount of the photoinduced *N* states decreases with increase of the distance from the sample surface depending on the number of the absorbed photon of the pump lights. Concerning these spectral features of $\Delta R/R$, detail analyses will be presented in Sec. VI A. Since the overall spectral shape of $\Delta R/R$ is quite similar to the calculated differential spectrum, we can consider that the obtained $\Delta R/R$ signals for $t_d = 20$ ps are also due to the photoinduced *N* states. When the excitation density is changed in the range of $0.01 - 1.2 \times 10^{16}$ photons/cm^2 or the temperature is in-

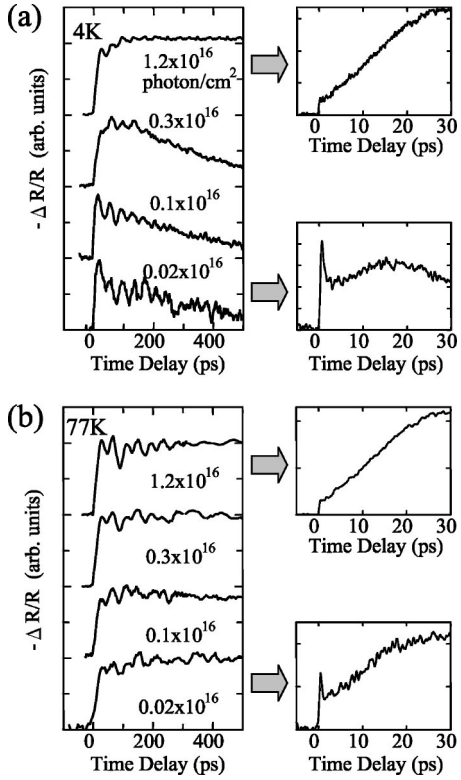

FIG. 4. Time evolutions of the transient reflectivity changes $(-\Delta R/R)$ measured at 2.25 eV for $\mathbf{E}\perp\mathbf{a}$; (a) 4 and (b) 77 K. The energy of the pump light ($\mathbf{E}\|\mathbf{a}$) is set to be 0.65 eV. The right side panels show the dynamics in the short time region.

creased to 77 K, the obtained $\Delta R/R$ spectra are essentially the same as the differential reflectivity spectrum, $[R_N(90\text{ K})-R_I(4\text{ K})]/R_I(4\text{ K})$, although there is a small difference of the spectral shape between them as mentioned earlier.

To discuss the dynamics of the photogenerated N states, we present the time evolutions of $-\Delta R/R$ at 4 and 77 K in Figs. 4(a) and 4(b), respectively. The detection energy is set to the peak energy (2.25 eV) of the intramolecular transition of TTF in the I phase, so that the decrease of R (or the increase of $-\Delta R/R$) indicates the generation of the N states. The $-\Delta R/R$ signals are accompanied by the prominent oscillations with the period of several tens of ps. The origin of these oscillations will be discussed later. The initial responses are presented in the right-hand figures of Fig. 4(a) and 4(b). At 4 K, the time characteristics strongly depend on the excitation density [see the left panel of Fig. 4(a)]. For the low excitation density ($N_{\text{ex}}=0.02\times10^{16}$ photons/cm^2), the initial rise of the signal is very fast as seen in the right lower panel of Fig. 4(a). The rise time τ_r is less than the time resolution of our system ($\sim$200 fs). The initial rise is accompanied by a sharp drop up to 2 ps and then the signal decays with the decay time of about 300 ps. For the high excitation density ($N_{\text{ex}}=1.2\times10^{16}$ photons/cm^2), we also observe the fast initial rise that is, however, followed by the drastic increase of the signal. Such an increase saturates at $t_d\sim20$ ps, but the signal does not decay at least to 500 ps.

At 77 K just below T_c, on the other hand, the time evolutions of the signals are rather independent of the excitation

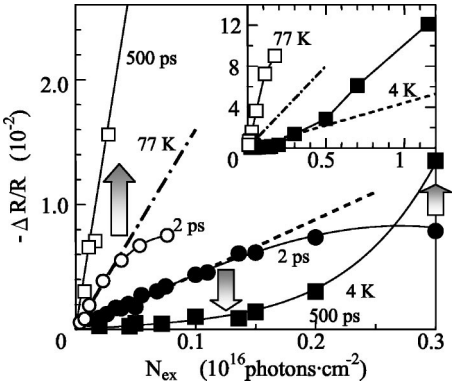

FIG. 5. The photoinduced changes in reflectivity $(-\Delta R/R)$ at 2.25 eV for $\mathbf{E}\perp\mathbf{a}$ as a function of the excitation density N_{ex}; the closed circles: $T=4$ K and $t_d=2$ ps; the closed squares: $T=4$ K and $t_d=500$ ps; the open circles: $T=77$ K and $t_d=2$ ps; the open squares: $T=77$ K and $t_d=500$ ps. The energy of the pump light ($\mathbf{E}\|\mathbf{a}$) is set to be 0.65 eV. In the inset, only the squares are plotted.

density as seen in Fig. 4(b) that are characterized by the fast rise within 200 fs and the following increase to $t_d\sim20$ ps. The important feature of the dynamics at 77 K is that the signal never decays, even for low excitation density. Such a feature is in contrast with the fast decay with the decay time $\sim$300 ps at 4 K. The photogenerated stable N states are found to decay completely within the time much less than the pulse interval (1 ms) at both 4 and 77 K, although their decay time is dependent on the excitation density.

To clarify the excitation density N_{ex} dependence in the dynamics of the photoinduced N states, we plotted $-\Delta R/R$ at $t_d=2$ and 500 ps as a function of N_{ex} in Fig. 5.[28] The $-\Delta R/R$ values at $t_d=2$ ps indicate the magnitudes of the initial rise, which show the amount of the D^0A^0 pairs just after the photoirradiation. When N_{ex} is less than 0.15×10^{16} photons/cm^2, the initial rise is proportional to N_{ex} at 4 K as shown by the broken line. In the same region of N_{ex}, the signals almost disappear at $t_d=500$ ps which reflects the fact that the photoinduced N states decay with the decay time $\sim$300 ps. When N_{ex} exceeds 0.3×10^{16}/cm^2, the initial rise saturates and the signal at $t_d=500$ ps increases sharply indicating the multiplication of the N states. At 77 K, the initial rise also shows the linear dependence on N_{ex} (the dashed-dotted line) for small N_{ex} less than 0.05×10^{16} photons/cm^2 and the saturation for the larger N_{ex}. The N states produced just after the photoirradiation never decay but always multiply.

The saturated value of the signals $-\Delta R/R$ at $t_d=2$ ps ($\sim$0.008) is in common at 4 and 77 K. Therefore, it is reasonable to consider that the saturation of the initial rise is related with the space filling of the N states generated in the I stacks. Considering the space-filling effects, we can estimate the amount of the N states (D^0A^0 pairs) initially produced. Here, we assume that the saturation occurs when half of the molecules within the absorption depth l_p for the pump light is neutralized. This assumption is based upon the expectation that the amount of the N states will not exceed that of the I states, since the two CT processes, $D^+A^-\rightarrow D^0A^0$ and $D^0A^0\rightarrow D^+A^-$, balance with each other, both of which are resonantly excited by the 0.65 eV pump [see Fig. 2(a)]. Us-

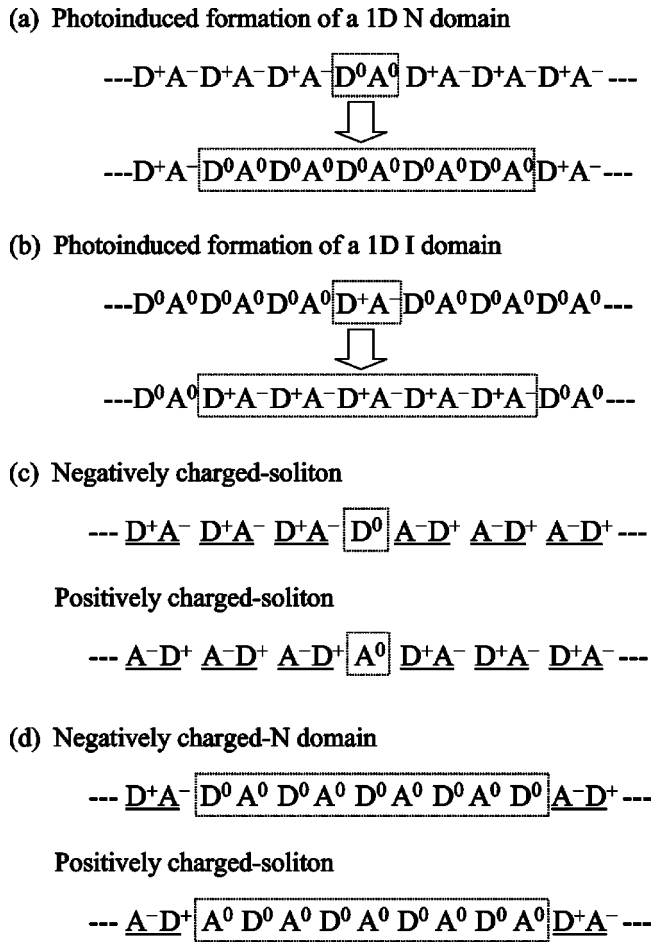

FIG. 6. (a) and (b) are schematic illustrations of photoinduced formations of a 1D *N* domain in the *I* phase and a 1D *I* domain in the *N* phase, respectively. (c) and (d) show charged-solitons and charged domains in the *I* phase, respectively.

ing the saturation densities ($N_s \sim 0.3 \times 10^{16}$ photons/cm^2 at 4 K and $\sim 0.1 \times 10^{16}$ photons/cm^2 at 77 K) and $l_p \sim 400$ Å, we can estimate the width of the initial *N* excited state, W_N, produced by one photon (a single CT excitation) to be 8 D^0A^0 pairs at 4 K and 24 D^0A^0 pairs at 77 K.

Since the results of the photoconductivity measurements shown in Fig. 2(b) demonstrate that the photocarriers are never generated by the resonant CT excitations, the photoexcited states will have excitonic character. Considering that the photoexcited state is composed of a number of D^0A^0 pairs, the photoexcited state is not attributable to a simple CT exciton but to a 1D confined *N* states, which will be relaxed from the Franck-Condon-type CT excited state. Formation process of the 1D confined *N* state is schematically illustrated in Fig. 6(a). Formation of the 1D *N* domain composed of a number of D^0A^0 pairs has been suggested from both theoretical[29–32] and experimental[9,33] points of view, when the *N* and *I* phases are almost degenerate. In the following, we will call the initial *N* state as a confined 1D *N* domain. The evaluated size of the confined 1D *N* domain at 77 K is larger than that at 4 K. This is perhaps because the valence instability is enhanced near T_c.

At 4 K, the initial confined 1D *N* domains decay rapidly for the low excitation density, while they are multiplied for

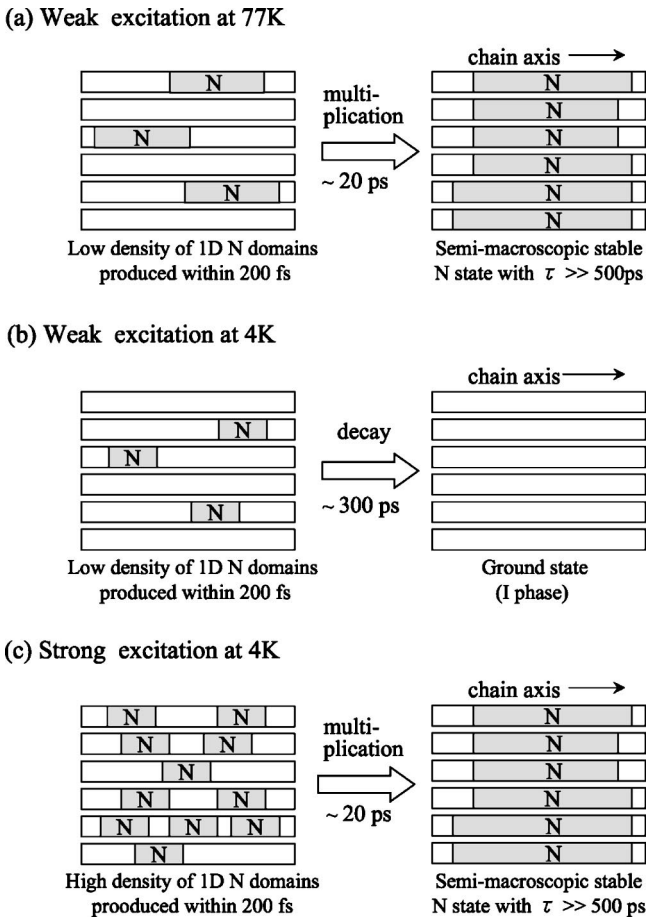

FIG. 7. Schematic illustrations of the photoinduced behaviors observed in the *I* phase; (a) the weak excitation at 77 K, (b) the weak excitation at 4 K, and (c) the strong excitation at 4 K.

the high excitation density. The *N* states produced after the multiplication have a lifetime much longer than 500 ps, suggesting the formation of the stable *N* states, which are different from the initial microscopic 1D *N* domains. It is reasonable to consider that the 1D *N* domains make the neighboring *I* states unstable and change them to *N* states, resulting in the production of semimacroscopic *N* states. The *I* phase in TTF-CA is stabilized by the interchain interactions as well as the intrachain one, as demonstrated by the detailed structural analysis.[13] As for the interchain interaction, there are two kinds of energy gain stabilizing the macroscopic *I* phase; one is due to the interchain Coulomb interaction, and the other to the three-dimensional (3D) ordering of dimeric displacements giving rise to the ferroelectric nature. Both energy gains will be lost by the generation of the confined 1D *N* domains. That would be the reason why the multiplication of the confined 1D *N* domains to the macroscopic *N* region occurs. The photoinduced behaviors for the low and high excitation densities observed at 4 K are schematically illustrated in Figs. 7(b) and 7(c), respectively.

At 77 K, the multiplication is observed for all the excitation densities we used. The lowest one is 0.005×10^{16} photons/cm^2, which corresponds to ~ 1 photon/1000 *DA* pairs. Such a promotion of the multiplication process of the *N* states at 77 K as well as the relatively large

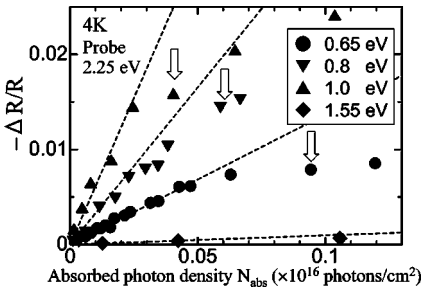

FIG. 8. The photoinduced changes of reflectivity ($-\Delta R/R$) at 2.25 eV ($\mathbf{E}\perp\mathbf{a}$) as a function of the absorbed photon density N_{abs} for various excitations ($\mathbf{E}\|\mathbf{a}$) ranging from 0.65 to 1.55 eV. The measurements were performed at 4 K. The broken lines give the linear relation between $-\Delta R/R$ and N_{abs}. The open arrows show the critical density at which the saturation of $-\Delta R/R$ occurs.

width of the initial confined 1D *N* domain is attributable to the enhancement of the valence instability near T_c. The photoinduced behavior for the low excitation density observed at 77 K is schematically illustrated in Fig. 7(a).

B. Excitation energy dependence of photoinduced *IN* transition

In the previous subsection, we report the photoinduced *IN* transition under the resonant CT excitation. The study about the excitation-energy dependence of the dynamics is indispensable for the overall understanding of the mechanism of the photoinduced *IN* transition.[34]

Figure 8 shows the absorption photon density N_{abs} dependence of $-\Delta R/R$ probed at 2.25 eV (4 K) for various excitation energies, which reflects the generation of the *N* states. N_{abs} is calculated from N_{ex} by considering the reflection loss. The absorption depth l_p for 1.55 eV ($l_p\sim 28\,000$ Å) is much longer than that for the other excitation energies (l_p ~ 400 Å for 0.65 eV, ~ 520 Å for 0.8 eV, and ~ 720 Å for 1.0 eV) and for the absorption depth of the probe light l_r (~ 1600 Å), so that the $-\Delta R/R$ signal for the 1.55 eV excitation is considerably smaller than that for the other three excitations. The magnitude of $-\Delta R/R$ is almost proportional to N_{abs}, when N_{abs} is low. In such low excitation densities, the time evolutions of $-\Delta R/R$ are independent of N_{abs} for each excitation energy. Typical time evolutions of $-\Delta R/R$ are presented in Fig. 9. As seen in Fig. 9, the decay of the photoinduced *N* states becomes slower with increase of the excitation energy. For the 1.55 eV excitation, the signal hardly decays up to 500 ps. In this excitation condition, the *N* states are never multiplied. Namely, the dynamics observed for the 1.55 eV excitation is completely different from those observed for the resonant (0.65 eV) excitation at 4 and 77 K shown in Fig. 4. The time characteristics of the *N* states in Fig. 9 can be reproduced by the sum of the component with the decay time $\tau=300$ ps and the constant term; $A\exp(-t/\tau)+B$. The constant term corresponds to the component with the decay time much longer than 500 ps. Its decay time was not exactly evaluated. However, it has been ascertained that the signal completely decays within the time much less than the pulse interval (1 ms). The amplitude of the slow decay component relative to the total amplitude of

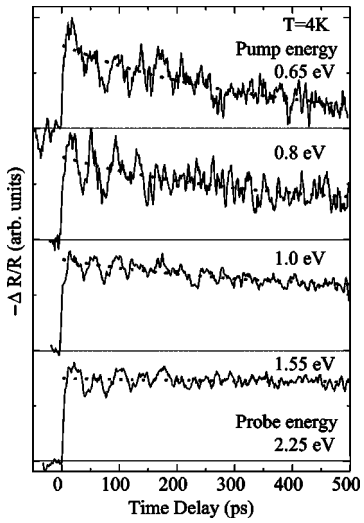

FIG. 9. Time evolutions of $-\Delta R/R$ at 2.25 eV ($\mathbf{E}\perp\mathbf{a}$) for various excitations ($\mathbf{E}\|\mathbf{a}$) ranging from 0.65 to 1.55 eV at 4 K. The excitation density is set to be very low, in which the dynamics is independent of the excitation density (see text).

the signal $[B/(A+B)]$ is plotted by the solid squares as a function of the excitation energy in Fig. 10, together with the ϵ_2 spectrum along the *DA* stack at 77 K (the solid line). With increase of the excitation energy, the ratio of the slow decay component gradually increases, indicating that the nature of the initial excited states changes depending on the excitation energy. As discussed earlier, the initial excited state for the 0.65 eV excitation is the confined 1D *N* domain, which decays with the decay time $\tau\sim 300$ ps and almost disappears at $t_d=500$ ps. Taking account of the excitation profile of the photoconductivity, the higher-energy excitation will generate positively and negatively charged species. In Fig. 10, the excitation profile of the photoconductivity in the *I* phase is replotted by the broken line. The excitation energy dependence of the slow decay component (the solid squares) is similar to that of the photoconductivity. It suggests that the *N* states having net charges are generated by the higher energy excitation and they have long lifetime.

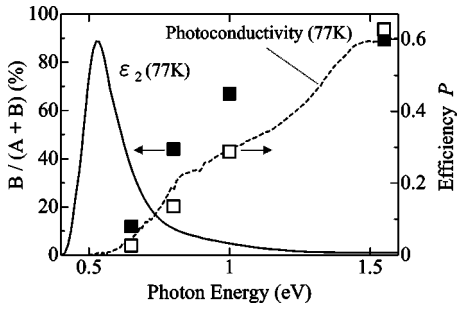

FIG. 10. The amplitudes of the slow decay components relative to the total amplitudes of the signal $[B/(A+B)]$ as a function of the excitation energy (the solid squares) obtained from the results in Fig. 9. The solid line is the ϵ_2 spectrum for $\mathbf{E}\|\mathbf{a}$ and the broken line is the excitation profile of the photoconductivity for $\mathbf{E}\|\mathbf{a}$ and $\mathbf{F}\|\mathbf{a}$ in the *I* phase at 77 K. The open squares show the generation efficiency of the charged *N* domains evaluated by assuming that the size of a charged *N* domain is 20 D^0A^0 pairs.

As the nature of the initial excited states changes depending on the excitation energy, the spatial size of the initial N state will also be varied. By assuming again that the saturation of the $-\Delta R/R$ signal occurs when half of the molecules within the absorption depth l_p is neutralized, we evaluated the size of the initial N state from the saturation photon density indicated by the arrows in Fig. 8. The evaluated size is ~ 17 D^0A^0 pairs for the 0.8 eV excitation and ~ 35 D^0A^0 pairs for the 1.0 eV excitation. These values are the average size of the initial N states composed of the noncharged N domains (the confined 1D N domains) and the charged N states. The size of the former is ~ 8 D^0A^0 pairs $(=W_N)$ at 4 K as mentioned earlier. Judging from the excitation energy dependence of $B/(A+B)$ shown in Fig. 10, the size of the latter $(=W_C)$ is expected to be slightly larger than 35 D^0A^0 pairs. The photoconductivity reflects the probability of the carrier separation P, while $B/(A+B)$ is expressed as $W_C/[W_CP+W_N(1-P)]$. Taking account of this relation, we can estimate the size of the charged N state (W_C) so that the excitation energy dependence of the carrier generation probability P is equal to that of the photoconductivity. When we set W_C to be 40 D^0A^0 pairs, the values of P are calculated as shown by the open squares in Fig. 10, the excitation energy dependence of which is in good agreement with that of the photoconductivity. The important point is that the spatial size of the charged N state is much larger than that of the noncharged N state (the confined 1D N domain) produced by the resonant excitation.

The charged carriers will be converted to charged N domains, probably during the carrier separation process. In other words, the charge carrier injection (or equivalently the injection of D^0 and A^0) in the I phase makes the neighboring I molecules unstable and then a relatively large size of 1D N domain is produced. Previous theoretical studies about the TTF-CA revealed that a possible charged excited state in the ionic phase is a charged soliton,[31] which is schematically illustrated in Fig. 6(c). When the energy of the N phase is close to that of the I phase, the energy gain of the Coulomb interaction by the charge will overcome the energy cost for the generation of the N states (D^0A^0 pairs). As a result, the width of the charged soliton is expected to increase as shown in Fig. 6(d). Assuming that the sizes of the positively- and negatively-charged N states are equal to each other, the size of the charged-soliton-like N state is estimated to be ~ 20 D^0A^0 pairs, since the total size of the charged N state is ~ 40 D^0A^0 pairs as mentioned earlier. It should be noted that the charged N state is composed of the odd number of neutral molecules, as shown in Fig. 6(d). Such a large size of the charged N state manifests that the charge-carrier injection shown in Fig. 6(c) makes the neighboring I states more unstable than the excitation of the CT exciton (or a D^0A^0 pair). The 1D charged-excited state will be strongly bound to the lattice due to its net charge, as compared with the 1D N domain with no charge. This may be the reason why the lifetime of the charged N states generated by the higher energy excitation is much longer than that of the confined 1D N domains generated by the resonant CT excitation as seen in Fig. 9.

When the excitation density is increased further for the higher energy excitations of 0.8 and 1.0 eV, the $-\Delta R/R$ signals just after the photoirradiation saturate as shown in Fig. 8, similarly to the result for the resonant (0.65 eV) excitation. In these cases, multiplications of the N states are also found to occur within about 30 ps and stable N states are produced.

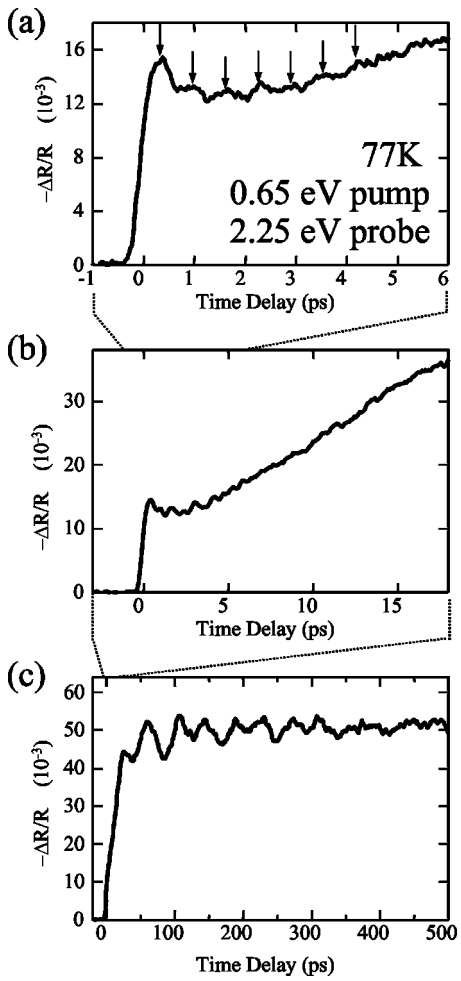

FIG. 11. Time evolutions of $-\Delta R/R$ at 2.25 eV ($\mathbf{E}\perp\mathbf{a}$) in the time regions of 0–6 (a), 0–18 (b), and 0–500 ps (c) in the I phase at 77 K. The pump energy is 0.65 eV ($\mathbf{E}\|\mathbf{a}$) and the pump density N_{ex} is 0.3×10^{16} photons/cm^2. The arrows indicate the coherent oscillation.

C. Coherent oscillations

In this subsection, we focus on the coherent oscillations observed on the photoinduced reflectivity changes, $\Delta R/R$, associated with the I to N conversion. Figures 11(a)–11(c) show the time characteristics of $-\Delta R/R$ for the 0.65 eV excitation $(0.3\times10^{16}$ photons/cm$^2)$ at 77 K in three typical time domains, 0–6, 0–18, and 0–500 ps, respectively. In Fig. 11(a), a rapid oscillation is observed as indicated by the arrows. In Fig. 12(a), we expand the time domain of 0–3 ps. By subtracting the background rise and decay from the time profile and performing a smoothing, the oscillatory component is obtained as shown in Fig. 12(b), in which an oscillation with the period of about 0.6 ps is clearly observed. The similar oscillations are also detected at 4 K for the 0.65 eV

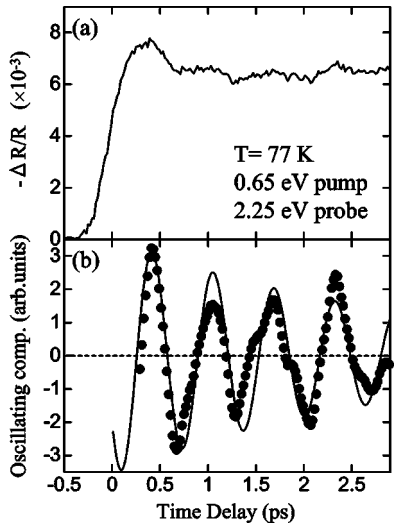

FIG. 12. (a) Initial response of the reflectivity change $(-\Delta R/R)$ shown in Fig. 11(a). (b) The oscillatory component obtained by subtracting background rise and decay from the time profile in (a) (the solid circles). The solid line shows a profile of a damped oscillator (see text).

excitation $(1.5\times10^{15}$ photons/cm$^2)$ as shown in Figs. 13(a) and 13(b). Amplitude of the oscillation is found to depend strongly on the probe energy. The amplitude of the first maximum of the oscillation indicated by the arrow in Fig. 13(b) is plotted for various probe energies in Fig. 13(c).

As detailed in Sec. IV A, the confined 1D *N* domains are multiplied at 77 K and then the semimacroscopic stable *N* state is produced within ~20 ps, which is reflected by the increase of the $-\Delta R/R$ signal shown in Fig. 11(b). After such semimacroscopic *N* state is stabilized, other oscillations with the periods of several tens of ps are found in the time evolution of $-\Delta R/R$, as seen in Fig. 11(c). Such oscillations are observed for the probe energies from 1.8 to 2.5 eV and at all the temperatures below T_c in common. To see clearly these oscillations, we subtracted the background rise and decay from the time profiles obtained for the 0.65 eV excitation $(1.2\times10^{16}$ photons/cm$^2)$ at 77 K. Figure 14 shows the residual oscillatory components at several typical energies of the probe lights. The obtained oscillatory components are composed of two oscillations having different periods. Moreover, the periods of the oscillations seem to change depending on the probe energies. The detail analyses of these coherent oscillations are presented in Sec. VI B.

V. PHOTOINDUCED *N* TO *I* TRANSITION

In this section, we will present the results of the p-p reflection spectroscopy associated with the photoinduced *N* to *I* transition. Figure 15(a) shows the spectra of the photoinduced reflectivity change $\Delta R/R$ at 90 K (the *N* phase) for the resonant CT excitation (0.65 eV) with $N_{\rm ex}=0.77\times10^{16}$ photons/cm^2. Taking into account the values of l_p ~510 Å and the reflection loss of 59%, this excitation density is estimated to be ~0.15 photon/*DA* pair. The spectral shapes of $\Delta R/R$ at $t_d=0-10$ ps are almost unchanged. In

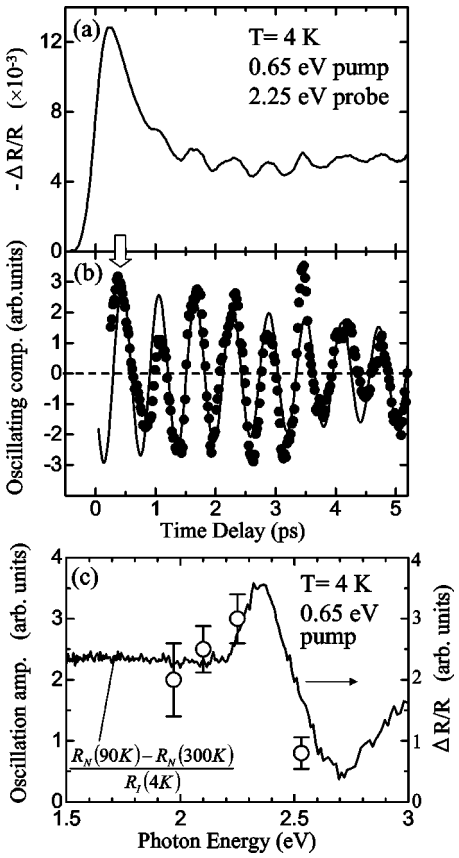

FIG. 13. (a) Initial response of the reflectivity change $(-\Delta R/R)$ at 2.25 eV $(\mathbf{E}\perp\mathbf{a})$ measured at 4 K. The pump energy is 0.65 eV $(\mathbf{E}\|\mathbf{a})$ and the pump density $N_{\rm ex}$ is 1.5×10^{15} photons/cm^2. (b) The oscillatory component obtained by subtracting background rise and decay from the time profile in (a) (the solid circles). The solid line shows a profile of a damped oscillator (see text). (c) The open circles show the probe energy dependence of the initial amplitudes of the oscillation indicated by the open arrow in (b). The solid line is the differential spectrum $[R_N(90\ {\rm K})-R_N(300\ {\rm K})]/R_I(4\ {\rm K})$.

Fig. 15(a), the solid line is the differential spectrum, $[R_I(4\ {\rm K})-R_N(90\ {\rm K})]/R_N(90\ {\rm K})$, calculated from the reflectivity spectra in the *I* phase at 4 K, $R_I(4\ {\rm K})$, and the *N* phase at 90 K, $R_N(90\ {\rm K})$. The $\Delta R/R$ spectrum at $t_d=0-10$ ps is almost equal to the $[R_I(4\ {\rm K})-R_N(90\ {\rm K})]/R_N(90\ {\rm K})$ spectrum except for in the high-energy region (2.3–2.6 eV). This difference is an artifact due to the change of the amount of the photoinduced *I* states depending on the distance from the sample surface. The details about the effects of such inhomogeneity on the spectral shape will be discussed in Sec. VI A. The observed $\Delta R/R$ spectra can be considered to reflect the photogeneration of the *I* state in the *N* phase. For $t_d=500$ ps, on the other hand, the $\Delta R/R$ signal is negative. Its spectral shape is completely different from the $[R_I(4\ {\rm K})-R_N(90\ {\rm K})]/R_N(90\ {\rm K})$ spectrum.

Figures 16(a) and 16(b) show the time characteristics of $\Delta R/R$ at 2.25 eV for several typical excitation densities, which reflect the amounts of the *I* states in the *N* phase. In each time characteristic, there is a fast rise within the time resolution, which decays very fast up to ~20 ps. Figure

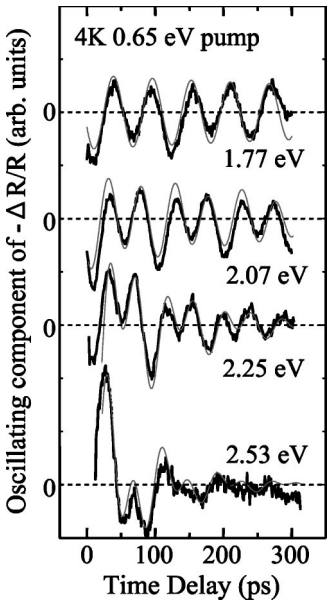

FIG. 14. Oscillatory components of the reflectivity change $(-\Delta R/R)$ for various probe energies ($\mathbf{E}\perp\mathbf{a}$) at 77 K. The pump energy is 0.65 eV ($\mathbf{E}\|\mathbf{a}$) and the excitation density is 1.2×10^{16} photons/cm^2.

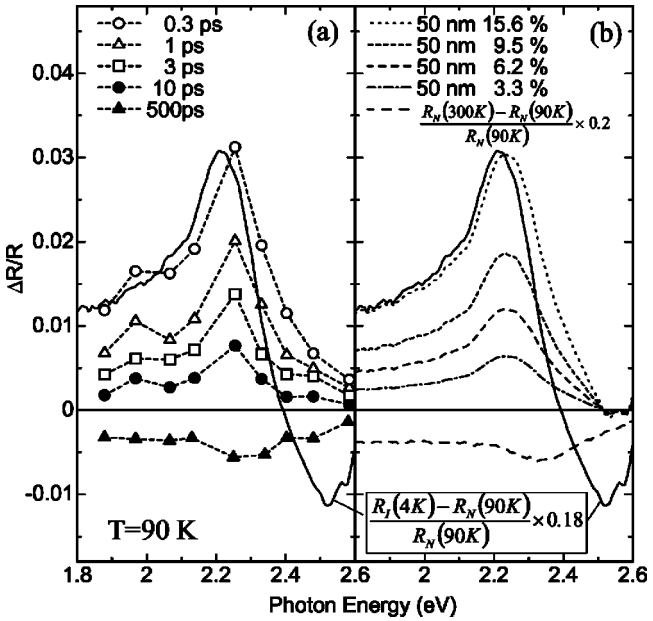

FIG. 15. (a) Transient differential reflection spectra $(\Delta R/R)$ in the intramolecular transition region measured with $\mathbf{E}\perp\mathbf{a}$ at 90 K for various time delays. The energy of the pump light ($\mathbf{E}\|\mathbf{a}$) is set to be 0.65 eV (the resonant CT excitation). Excitation density is 0.77×10^{16} photons/cm^2. The solid line shows the differential spectrum, $[R_I(4\text{ K})-R_N(90\text{ K})]/R_N(90\text{ K})$. (b) The differential reflection spectra $(\Delta R/R)$ calculated by using the multilayer model. The used parameters β^{-1} (nm) and x_0 (%) are listed in the figure. The broken line is the differential spectrum, $[R_N(300\text{ K})-R_N(90\text{ K})]/R_N(90\text{ K})$.

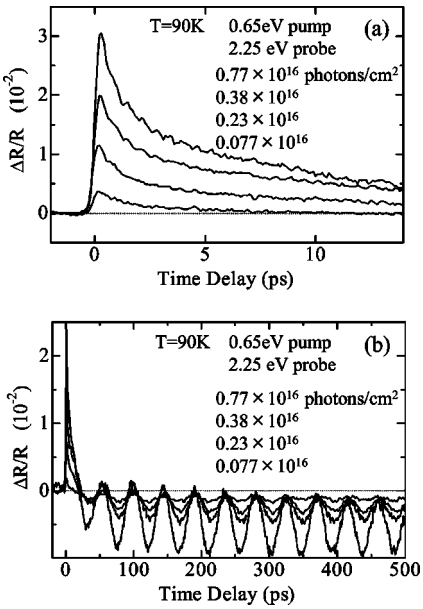

FIG. 16. Time characteristics of the photoinduced reflectivity changes $\Delta R/R$ at 2.25 eV ($\mathbf{E}\perp\mathbf{a}$) at 90 K for several typical excitation densities; (a) short time region; (b) long time region. The energy of the pump light ($\mathbf{E}\|\mathbf{a}$) is set to be 0.65 eV.

17(a) is the magnified time profile in 0–5 ps for the excitation density $N_{ex}=0.9\times10^{16}$ photons/cm^2. A rapid oscillation is clearly observed. The oscillatory component obtained by subtracting the background rise and decay and performing a smoothing is presented in Fig. 17(b). The period of the oscillation is about 0.6 ps. Amplitude of this oscillation is also dependent on the probe energy, similarly to the oscillation with the period of ~0.6 ps in the I phase. The amplitude of the first maximum of the oscillation indicated by the arrow in Fig. 17(b) is plotted for various photon energies in Fig. 17(c). In addition to the rapid oscillation, more prominent oscillation with the period of about 50 ps is observed as seen in Fig. 16(b). As for these two kinds of coherent oscillations observed in the $\Delta R/R$ signals, we will give detailed discussions in Sec. VI B.

When excluding the oscillatory component with the period of about 50 ps in Fig. 16(b), we can see that $\Delta R/R$ changes its sign around $t_d=20$ ps and becomes negative, and then saturates around $t_d=100$ ps. For $t_d>100$ ps, the signal is almost constant at least up to 500 ps.

In Fig. 18(a), the excitation density N_{ex} dependence of the $\Delta R/R$ signals at $t_d=0.3$ and 500 ps is presented. The $\Delta R/R$ signals at $t_d=0.3$ ps are almost proportional to N_{ex} up to 0.4×10^{16} photons/cm^2 and then saturate. We have also estimated the width of the initial I state $(=W_I)$ from the saturation photon density N_s. Using $N_s\sim0.5\times10^{16}$ photons/cm^2, $l_p\sim510$ Å, and the reflection loss of 0.59, W_I is estimated to be about 5 D^+A^- pairs. As seen in Fig. 2(b), in the N phase, the charge carriers are not generated by the resonant CT excitation as well as in the I phase, so that the confined I domains[35] will be generated by lights. The formation process of the confined I domain is illustrated in Fig. 6(b).

The magnitudes of the negative signals of $\Delta R/R$ at $t_d=500$ ps, on the other hand, start to saturate at very low

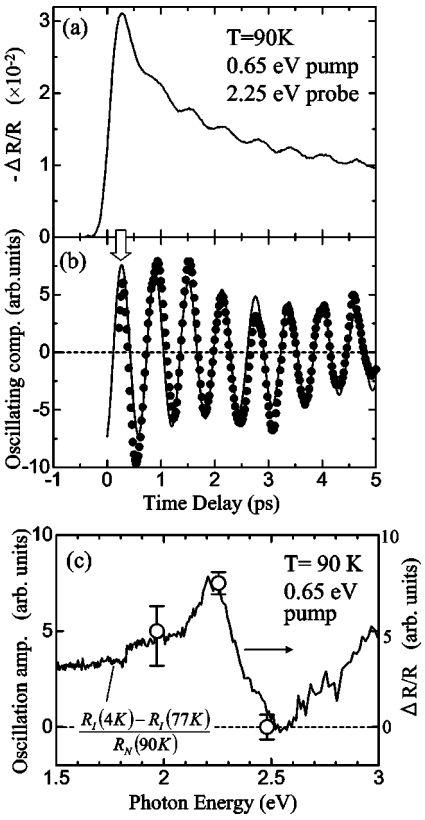

FIG. 17. (a) Initial response of the reflectivity change ($\Delta R/R$) at 2.25 eV ($\mathbf{E}\perp\mathbf{a}$) at 90 K. The pump energy is 0.65 eV ($\mathbf{E}\|\mathbf{a}$) and the pump density N_{ex} is 0.9×10^{16} photons/cm^2. (b) The oscillating component obtained by subtracting background rise and decay from the time profile in (a) (the solid circles). The solid line shows a profile of a damped oscillator (see text). (c) The open circles show the probe energy dependence of the initial amplitudes of the oscillation indicated by the open arrow in (b). The solid line is the differential spectrum $[R_I(4\text{ K})-R_I(77\text{ K})]/R_N(90\text{ K})$.

excitation density (0.2×10^{16} photons/cm^2) as seen in Fig. 18(a). A most plausible origin of the negative signals is a thermal effect. To evaluate the thermal effect, we calculate the differential spectrum, $[R_N(300\text{ K})-R_N(90\text{ K})]/R_N(90\text{ K})$, which is shown by the broken line in Fig. 15(b). $[R_N(300\text{ K})-R_N(90\text{ K})]/R_N(90\text{ K})$ is found to be negative over the wide energy range. Its spectral shape is almost equal to the $\Delta R/R$ spectrum at $t_d=500$ ps experimentally obtained.

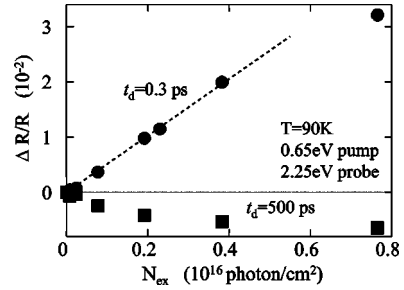

FIG. 18. The excitation density N_{ex} dependence of the $\Delta R/R$ signals at $t_d=0.3$ and 500 ps (90 K, 0.65 eV excitation with $\mathbf{E}\|\mathbf{a}$). The broken line shows the linear relation between $\Delta R/R$ and N_{ex}.

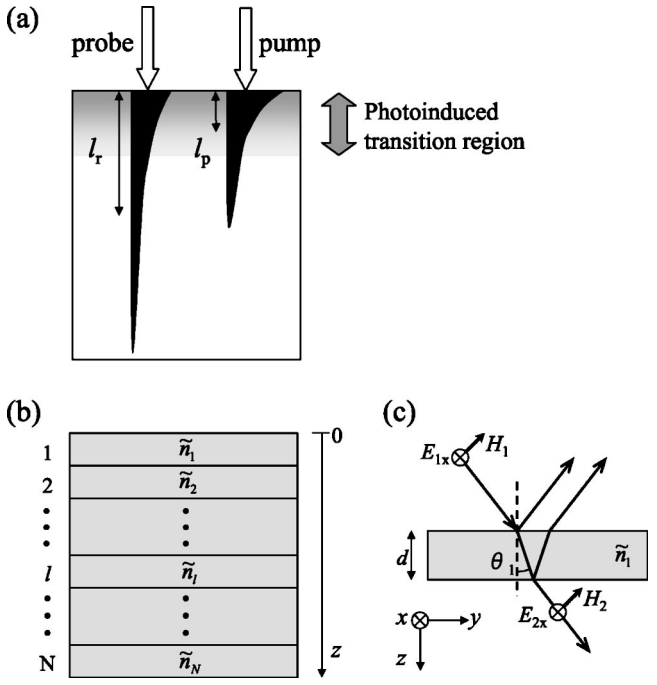

FIG. 19. (a) Schematic illustration of the difference of the absorption depths between the pump light (l_p) and the probe light (l_r). (b) Schematic illustration of the multilayer model. The sample is assumed to be composed of N layers with the complex refractive index $\tilde{n}_l$. The z axis is normal to the sample surface. (c) The definitions of electric and magnetic fields of the incident light (E_{1x},H_{1y}) and the transmitted light (E_{2x},H_{2y}), and the angle of refraction (θ_1) associated with the first layer. d is the thickness of the layer.

These results suggest the following interpretation; the photoinduced I states decay within ~20 ps through the nonradiative processes and their energies are transferred to the lattice. Then the lattice temperature is increased and the spectral change corresponding to the sample heating is observed for $t_d>30$ ps.

As seen in Figs. 16(a) and 16(b), the decay time of the photoinduced I states is very small and there is no indication of multiplication of the I states, when the excitation density is increased. It has been ascertained that these features are almost independent of the excitation energy from 0.65 to 1.55 eV. It is clear that there is a significant difference of the dynamical behaviors between the photoinduced *IN* and *NI* transitions.

VI. DISCUSSIONS

A. Analysis of transient reflectivity changes

1. Multilayer model

When a single crystal sample is irradiated by light, the amount of the photoexcited states or carriers is exponentially decreased with increase of the distance from the sample surface. In addition, in the reflection detected p-p measurement used here, absorption depths of the probe light (l_r) are dependent on its energy and different from that of the pump

light (l_p) as illustrated in Fig. 19(a). Such inhomogeneity of the carrier concentration and the difference between l_p and l_r should affect magnitude and spectral shape of transient reflectivity changes, $\Delta R/R$.[36–38] Moreover, in the case that photoexcited species just after the photoirradiation are multiplied with time as observed in the photoinduced *IN* transition of TTF-CA, the distribution of the photoexcited species in the direction normal to the sample surface may be dependent on time. In the previous section, we neglected these effects, so that the presented discussions are so qualitative. Here, we present precise analysis of the spectral shape and magnitude of $\Delta R/R$, in which the time-dependent inhomogeneity in the concentration of photoexcited states is taken into account in the variation of refractive index and the absorption-depth difference is exactly treated. From the analysis, we can derive detailed information about the dynamics of the photoinduced *IN* and *NI* transitions.

To analyze $\Delta R/R$ spectra, we adopt a multilayer model.[39] In this model, we consider that a material is composed of many thin layers having different optical constant (the complex refractive index $\tilde{n}$), as shown in Fig. 19(b). $\tilde{n}_l$ is assumed to be constant within the lth layer. Reflectivity R of such a multilayer can be easily calculated. When we apply this model to the analysis of $\Delta R/R$ spectra, we adopt the following assumptions.

(1) The value of $\tilde{n}$ in each layer is expressed as $\tilde{n}=C_I\tilde{n}_I+C_N\tilde{n}_N$, $(C_I+C_N=1)$. Here, $\tilde{n}_I$ and $\tilde{n}_N$ are the refractive index of the I phase and the N phase, respectively. C_I and C_N are the ratio of the I and N states (or I and N molecules), respectively.

(2) The value of C_N (C_I) in the photoinduced *IN* (*NI*) transition is expressed by the exponential function of the distance z from the sample surface along the normal direction to the surface as C_N $(C_I) \propto \exp(-\beta z)$.

The size of each N domain photogenerated in the I phase (or I domain photogenerated in the N phase) will be considerably smaller than the wavelength of the probe lights. In such a case, assumption (1) will be valid. Assumption (2) comes from the fact that the number of the absorbed photons decreases exponentially with increase of z. As discussed in Sec. IV, in the case of the photoinduced *IN* transition, it depends on the excitation density N_{ex} whether the photoexcited N states are multiplied or decayed. Therefore, the distribution of the N states is not necessarily equal to that of the absorbed photons determined by the absorption coefficient α_p, but is changed with time. In our model, such nonlinear effects can be taken into account through the change of the characteristic length $1/\beta$ by considering β as a time-dependent fitting parameter.

In the following, we go on with discussions in the case of the photoinduced *IN* transition. The treatment for the photoinduced *NI* transition is completely the same. According to the assumptions mentioned above, C_I and C_N are given as follows:

$$C_I(z) = 1 - x_0 \exp(-\beta z),$$

$$C_N(z) = x_0 \exp(-\beta z).$$

Here, x_0 is the density of the photoinduced N state at the sample surface $(z=0)$. The refractive index $\tilde{n}(z)$ is expressed as

$$\tilde{n}(z) = \tilde{n}_I\{1 - x_0 \exp(-\beta z)\} + \tilde{n}_N x_0 \exp(-\beta z).$$

Each layer with the width of d is labeled by $1 \sim N$, as shown in Fig. 19(b). The refractive index $\tilde{n}_l$ of the lth layer is expressed as follows:

$$\tilde{n}_l = \tilde{n}_I[1 - x_0 \exp\{-\beta(l-1)d\}] + \tilde{n}_N x_0 \exp\{-\beta(l-1)d\}.$$

Let us consider that the TE mode of the light passes through the film with the refractive index $\tilde{n}_1$, as illustrated in Fig. 19(b). θ_1 is the angle of refraction. In this case, the electric field E_{1x} and the y component of the magnetic field H_{1y} of the incident light, (E_{1x},H_{1y}), are connected with those of the transmitted light, (E_{2x},H_{2y}), by the matrix M_1 as follows:

$$\begin{pmatrix} E_{1x} \\ H_{1y} \end{pmatrix} = M_1 \begin{pmatrix} E_{2x} \\ H_{2y} \end{pmatrix} = \begin{pmatrix} \cos k\Delta_1 & \dfrac{-i \sin k\Delta_1}{p_1} \\ -ip_1 \sin k\Delta_1 & \cos k\Delta_1 \end{pmatrix} \begin{pmatrix} E_{2x} \\ H_{2y} \end{pmatrix}.$$

Here, $\Delta_1=\tilde{n}_1 d \cos\theta_1$ and $p_1=\sqrt{\epsilon_0/\mu_0}\tilde{n}_1 \cos\theta_1$. k is the wave number of the incident light in vacuum. A similar relation stands for the lth layer

$$\begin{pmatrix} E_{lx} \\ H_{ly} \end{pmatrix} = M_l \begin{pmatrix} E_{l+1x} \\ H_{l+1y} \end{pmatrix} = \begin{pmatrix} \cos k\Delta_l & \dfrac{-i \sin k\Delta_l}{p_l} \\ -ip_l \sin k\Delta_l & \cos k\Delta_l \end{pmatrix} \begin{pmatrix} E_{l+1x} \\ H_{l+1y} \end{pmatrix}.$$

Here, $\Delta_l=\tilde{n}_1 d \cos\theta_l$ and $p_l=\sqrt{\epsilon_0/\mu_0}\tilde{n}_l \cos\theta_l$. θ_l is the angle of refraction. We consider the matrix M defined as

$$M = M_1 M_2 M_3 \cdots M_N,$$

$$M = \begin{pmatrix} m_{11} & m_{12} \\ m_{21} & m_{22} \end{pmatrix}.$$

The reflectivity R of the N-layer sample is expressed by using the elements of the matrix M, and the parameters p_1 and p_N as follows:

$$R = \left| \frac{(m_{11} + m_{12}p_N)p_1 - (m_{21} + m_{22}p_N)}{(m_{11} + m_{12}p_N)p_1 + (m_{21} + m_{22}p_N)} \right|^2.$$

In our case, the direction of the incident light is almost perpendicular to the sample surface, so that θ_l can be set to be zero.

2. Analysis of transient reflectivity changes in photoinduced IN transition

Using the multilayer model presented earlier, we have tried to reproduce the differential reflectivity spectra $\Delta R/R$ in Fig. 3(a), which are measured at 4 K with the resonant (0.65 eV) excitation of the CT band. $\tilde{n}_I$ and $\tilde{n}_N$ were deduced by applying the KK transformation to the polarized reflectivity spectra at 4 and 90 K, respectively, which are shown in Fig. 2(a). The adjustable parameters in our model are, therefore, only two parameters, that is, β and x_0.

First, we set the total thickness of the analyzed region to be 5000 Å, which is much larger than the absorption depths of the probe lights l_r in the intramolecular transition region from 1.8 to 2.6 eV for $\mathbf{E} \perp \mathbf{a}$ (1300–3200 Å) and that of the pump light l_p (~400 Å). Next, the sample with the thickness

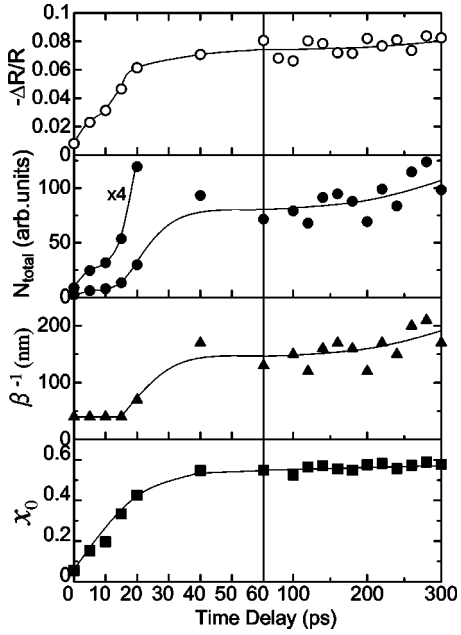

FIG. 20. Time characteristics of $-\Delta R/R$ at 2.25 eV ($\mathbf{E}\perp\mathbf{a}$) at 4 K corresponding to the result of Fig. 3(a), and time characteristics of the total amounts of the N state (N_{total}), the characteristic length for the distribution of the N state (β^{-1}), and the ratio of the N state at the sample surface (x_0), which were obtained by the simulation based upon the multilayer model presented in Fig. 3(b).

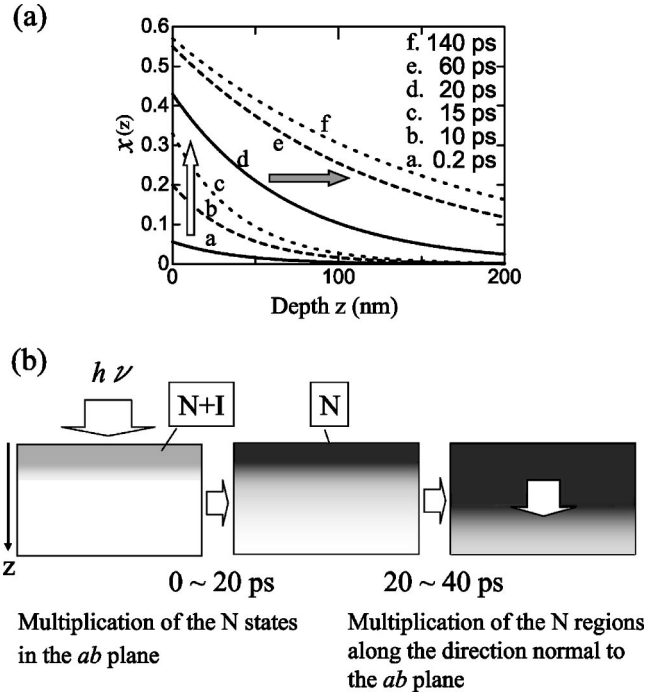

FIG. 21. (a) The time dependence of the ratio $x(z)$ of the N states in the photoinduced I to N transition. z is the distance from the sample surface. The white and gray arrows indicate the changes of the N states for $t_d<20$ ps and $t_d>20$ ps, respectively. (b) Schematic illustration of the multiplication process in the photoinduced I to N transition. Shade shows the coexistence of the N and I state and black region shows the N state.

of 5000 Å is divided to $N=1000$ layers with the thickness of $d=5$ Å. We have ascertained that the calculated spectra are not changed when the total thickness is increased larger than 5000 Å or d is decreased less than 5 Å.

The calculated $\Delta R/R$ spectra are presented in Fig. 3(b). As mentioned in Sec. IV, the spectral shape of the experimental $\Delta R/R$ signals in Fig. 3(a) shows the characteristic time dependence in the higher energy region around 2.5 eV, which is well reproduced by the calculated spectra. The used parameter values $1/\beta$ and x_0 are presented as a function of the delay time t_d in Fig. 20, together with $-\Delta R/R$ at 2.25 eV and the total amount of the photoinduced N state N_{total}. N_{total} is proportional to x_0/β. We can see several important features of the photoinduced IN transition from Fig. 20. For $t_d<20$ ps, x_0 gradually increases, while $1/\beta$ is almost unchanged. Namely, in this time region, the multiplication process of the N states generated just after the photoirradiation occurs two dimensionally in the plane parallel to the sample surface. N_{total}, therefore, increases being proportional to x_0. At $t_d>20$ ps, multiplication dynamics is considerably changed. At $t_d=20$ ps, $1/\beta$ starts to increase and saturates at around $t_d=40$ ps. At $t_d=20-40$ ps, x_0 continues to increase, although the slope of the x_0-t_d curve rather decreases. As a result, N_{total} remarkably increases during $t_d=20-40$ ps. For $t_d>40$ ps, the increase of x_0 becomes small, that is about only 5% from $t_d=40$ to 300 ps. The sharp increase of $1/\beta$ also stops at around $t_d=40$ ps. $1/\beta$ increases slightly ($\sim$20%) from $t_d=40$ to 300 ps.

From these results, the multiplication dynamics of the photoinduced N states can be interpreted as follows. For $t_d<20$ ps, the distribution of the N states along the direction perpendicular to the sample surface [$\|z$ in Fig. 19(b)] is the same as that just after the photoirradiation, which is proportional to $\exp(-\alpha_p z)$. The multiplications of the N states occur two-dimensionally in the plane parallel to the sample surface ($\perp z$). For $t_d>20$ ps, on the other hand, the two-dimensional multiplications near the sample surface saturate and the multiplications occur in the direction perpendicular to the sample surface ($\|z$). Such a multiplication process can be seen clearly in Fig. 21(a), in which the ratio of the photoinduced N states as a function of z, $x(z)$, is plotted for various t_d. Here, $x(0)=x_0$. These multiplication processes are also schematically illustrated in Fig. 21(b), in which the density of the photoinduced N states is shown by the shade.

3. Analysis of the differential reflectivity spectra in photoinduced NI transition

Using the multilayer model presented earlier, we have also analyzed the differential reflectivity spectra $\Delta R/R$ in Fig. 15(a), which are measured at 90 K with the resonant (0.65 eV) excitation of the CT band. As for the parameters $\tilde{n}_I$ and $\tilde{n}_N$, the refractive indexes at 4 and 90 K were used, respectively. The absorption depth l_p is $\sim$510 Å. The values of d and N are also set to be 5 Å and 1000, respectively.

We presented the calculated $\Delta R/R$ spectra in Fig. 15(b), which are in good agreement with the experimental results in

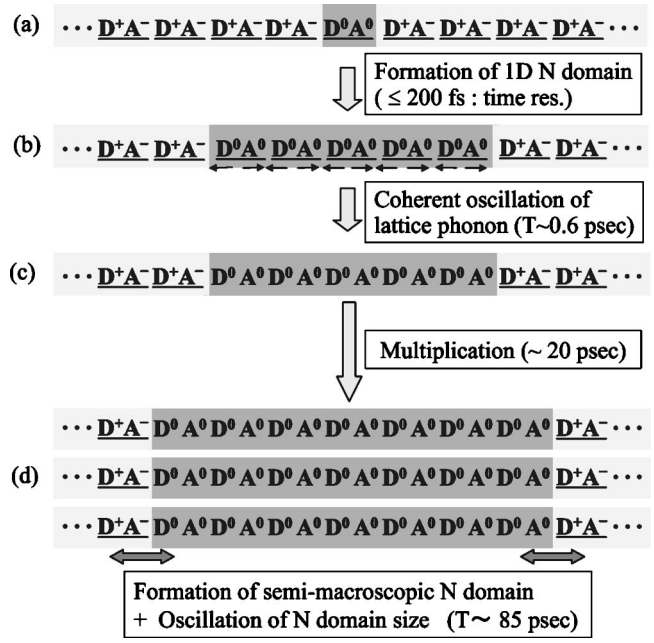

FIG. 22. Schematic illustration of the observed dynamics in the photoinduced *NI* transition (see text).

Fig. 15(a). In these calculations, $1/\beta$ is constant ($=l_p$) and x_0 changes from 15.6% ($t_d=0$ ps) to 3.3% ($t_d=10$ ps) as shown in the figure. Note that the spectral shape of $\Delta R/R$ at 2.3–2.6 eV, which is not equal to that of the differential spectrum, $[R_I(4\text{ K})-R_N(90\text{ K})]/R_N(90\text{ K})$, is completely reproduced. Such a difference is, therefore, conclusively attributed to the inhomogeneity of the refractive index within the absorption depth of the probe light. It has been ascertained that time characteristics of the amount of the photoinduced *I* state derived from this analysis are in good agreement with that of $\Delta R/R$.

B. Analysis of the coherent oscillations

1. Coherent oscillations in the photoinduced IN transition

In this subsection, we will discuss the coherent oscillation on the photoinduced signals associated with the photoinduced *IN* transition. First, we focus on the rapid oscillation shown in Figs. 12 and 13. This oscillatory component was analyzed by a damped oscillator represented by the following simple formula:

$$-\frac{\Delta R}{R}=A_0\cos(\omega_0 t-\phi_0)\exp(-t/\tau_0). \qquad (1)$$

In Figs. 12(b) and 13(b), the calculated time profile is shown by the solid line, which reproduces well the experimental result. The obtained frequency ω_1 (the period T) of this oscillation is $\sim$56 cm^{-1} ($\sim$0.60 ps). The decay time τ_0 of the oscillation is about 3.0 ps in Fig. 12(b) and 7.0 ps in Fig. 13(b). Taking into account the frequency value of the oscillation (56 cm^{-1}), it is natural to consider that this oscillation is related with an optical mode of lattice phonon.

The observed rapid oscillation can be qualitatively interpreted as illustrated in Fig. 22(a–c). A CT excited state is initially photogenerated [Fig. 22(a)]. Just after the photoirradiation, a confined 1D *N* domain composed of several D^0A^0 pairs is produced from the CT excited state [Fig. 22(b)]. This process corresponds to a sequence of the electron transfer processes, so that it will occur within the time scale of the transfer energy t. If t is assumed to be 0.1 eV, which is a typical value for the mixed-stack CT compounds, its time scale is $\sim$40 fs that is much faster than the time resolution ($\sim$200 fs). Therefore, the formation process of the confined 1D *N* domain cannot be resolved in time domain by our system. In the formation process of the 1D *N* domain, the dimeric molecular displacements will persist as shown in Fig. 22(b), since the time scale of the lattice phonon, that is 0.6 ps, is much longer than that of the transfer energy ($\sim$40 fs). In the confined 1D *N* domain, each molecule has no spin, so that the dimeric displacements should be dissolved. Remember that the molecular dimerization is caused by the SP instability. In the dissolution process of the dimeric molecular displacements, the coherent oscillation does occur as shown by the arrows in Fig. 22(b). This type of optical phonon is infrared (IR)-active independent of the lattice dimerizations but Raman-active only when the lattice is dimerized. In the previous IR and Raman studies, an IR mode is observed at around 58 cm^{-1} in both the *N* and *I* phases[40] and a Raman mode activated only in the *I* phase is observed at 57 cm^{-1}.[41] The phonon mode observed in these studies might correspond to the coherent oscillation detected here.

Such an oscillation will modulate the transfer energy between the neighboring *D* and *A* molecules. It is reasonable to consider that the value of the degree of charge-transfer ρ decreases with decrease of the dimeric displacements through the decrease of the intradimer transfer energy. As a result, the coherent oscillation modulates ρ and, then, is detected as the reflectivity change of the intramolecular transition sensitive to ρ.

The oscillations are of the confined 1D *N* domains. Therefore, their amplitudes should reflect the change of ρ in the *N* state. The solid line in Fig. 13(c) shows the differential reflectivity spectrum, $[R_N(90\text{ K})-R_N(300\text{ K})]/R_I(4\text{ K})$, which corresponds to the increase of ρ by $\sim$0.07 in the *N* phase.[19] The probe energy dependence of the amplitude of the oscillation shown by the open circles is very similar to the spectral shape of $[R_N(90\text{ K})-R_N(300\text{ K})]/R_I(4\text{ K})$. This fact strongly demonstrates the interpretation presented earlier. As seen in the solid line in Figs. 12(b) and 13(b), the initial phase of the oscillation defined by Eq. (1) is almost equal to π. This is also quite reasonable because ρ should decrease through the change from the dimerized *N* state [Fig. 22(b)] to the undimerized *N* state [Fig. 22(c)] as discussed earlier.

As mentioned in Sec. IV, the spike-like rise and decay is observed within 2 ps in the time evolution of $-\Delta R/R$ for the small excitation density [see the right lower panels of Figs. 4(a) and 4(b)]. It is natural to consider that these structures will also be related with the dynamical behavior of molecular displacements. In fact, the similar analyses have revealed that several periods of the coherent oscillation can be distinguished in the results for the low excitation density.

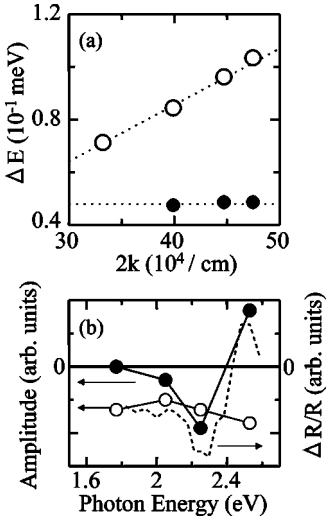

FIG. 23. (a) Quantum energy of the oscillation ($\Delta E=\hbar\omega$) observed in Fig. 14 as a function of $2k$; the closed circles: the low-frequency oscillation; the open circles: the high-frequency oscillation. k is the wave number of the probe light. (b) Amplitudes of the high-frequency oscillation (the open circles) and the low-frequency oscillation (the closed circles) as a function of the probe energy. The broken line is the $\Delta R/R$ spectrum at $t_d=500$ ps.

Next, we will discuss other coherent oscillations with the period of several tens of ps at 77 K, which are shown in Fig. 14. To analyze these oscillations, we have tried to fit the data by a superposition of two exponentially damped oscillations represented as follows:

$$-\frac{\Delta R}{R}=\sum_i A_i\cos(\omega_i t-\phi_i)\exp(-t/\tau_i):(i=1,2). \qquad (2)$$

The thin solid lines in Fig. 14 are the calculated results, which reproduce well the experimental ones. Figure 23(a) shows the quantum energy of the oscillation ($\Delta E=\hbar\omega$) as a function of the twice ($2k$) of the wave number of the probe lights k ($k=2\pi n/\lambda$) in the sample. In Fig. 23(b), the amplitudes of the low- and high-frequency oscillations are presented by the solid and open circles, respectively. In the low frequency oscillations, the phase (ϕ) is almost constant for the probe energies of 1.77–2.25 eV, but shifts relatively by π at 2.53 eV. Such a shift of π is taken into account as a change of the sign of the amplitudes in Fig. 23(b). In the high-frequency oscillations, on the other hand, ϕ is independent of the probe energy. As seen in Fig. 23(b), the observed two oscillations show apparently different behaviors.

The amplitudes of the high frequency oscillation [the open circles in Fig. 23(b)] are almost constant. ΔE rather depends on the probe energy, being proportional to k and the corresponding period changes from 37 to 57 ps. From these features, this oscillation is attributable to the shock wave, which is generated from the photoinduced impulsive mechanical stress. In the temperature induced *NI* transition, the unit cell volume decreases by about 0.6% across T_c.[13] Therefore, photoinduced *IN* conversion will also produce a sudden volume change, which acts as a broadband source of acoustic

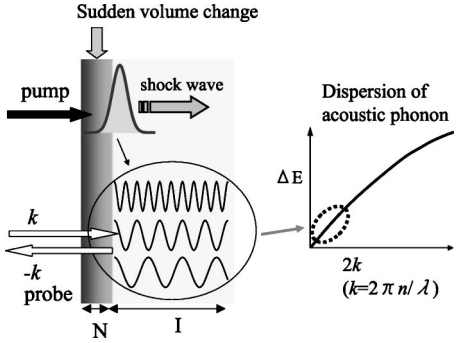

FIG. 24. Schematic illustrations of the shock wave and the dispersion of the acoustic phonon. The shock wave acts as a broadband source of acoustic phonons. The probe light having the wave number k is modulated by the coherent acoustic phonon with $2k$. ΔE as a function of $2k$ gives the dispersion of the acoustic phonon.

phonons.[42] In this case, the monochromatic probe light should be modulated by the phonon having the wave number $2k$. A relation between the modulation frequency and $2k$ corresponds to a dispersion of the acoustic phonon, which gives a linear relation for small k. The generation of the shock wave and the modulation of the probe light are schematically illustrated in Fig. 24. The observed linear relation between ΔE and $2k$ seen in Fig. 23(a) demonstrates that the observed high-frequency oscillation is attributed to a shock wave. The sound velocity is calculated to be 0.65×10^5 cm/s from the slope of the open circles in Fig. 23(a). Tanimura and Akimoto also detected the same oscillations in TTF-CA.[43] This kind of oscillation in the photoinduced reflectivity change has been previously reported in the study on the photoinduced melting of a charge-ordered state of perovskite manganite.[44]

As for the lower-frequency oscillation, ΔE does not depend on the probe energies as seen in Fig. 23(a) and the period of the oscillation is ~85 ps. The profile of the amplitudes is in good agreement with that of $-\Delta R/R$ shown by the broken line in Fig. 23(b). Therefore, this oscillation should be related with the change of the molecular ionicity ρ. A possible origin is a modulation in the amount of the N states. To investigate this possibility, we have calculated the power spectra from the time profiles of $-\Delta R/R(2.25\text{ eV})$ at various temperatures (not shown) by using the Fourier transformation procedures. The obtained power spectra are presented in Fig. 25(a). Intensity of the low-frequency band (I_l) relative to the high frequency band (I_h) is considerably enhanced with

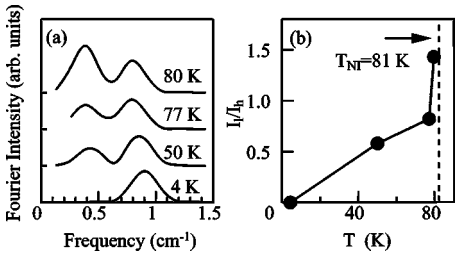

FIG. 25. (a) Fourier power spectra of the oscillatory components observed in Fig. 14 at various temperatures. (b) The ratio between the amplitudes of low- (I_l) and high-frequency peak (I_h).

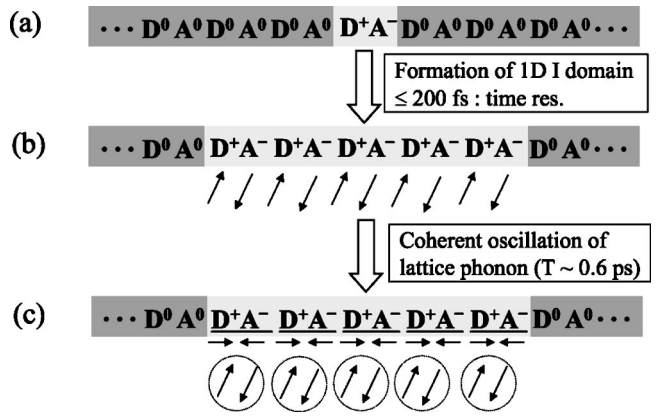

FIG. 26. Schematic illustration of the observed dynamics in the photoinduced *NI* transition (see text).

increase of temperature up to T_c as shown in Fig. 25(b). From the result, we can consider that the low frequency oscillation is related with the valence instability, and, therefore, is attributed to the modulation in the amount of the *N* states. It should be noted that this oscillation starts at $t_d \sim 20$ ps just after the multiplication of the confined 1D *N* domains to the semimacroscopic *N* state is completed. This indicates that the observed oscillation is not due to the confined 1D *N* domains initially photogenerated. The modulation in the size of the semimacroscopic *N* domain, or equivalently, the coherent motion of the *NI* domain boundary over the macroscopic scale will be responsible for the low frequency oscillation, that is schematically illustrated in Fig. 22(d).

2. Coherent oscillations in photoinduced NI transition

As mentioned in Sec. V, there are also observed two kinds of coherent oscillations in the photoinduced *NI* transition, which are shown in Figs. 16(b), 17(a), and 17(b). The oscilatory component in the picosecond region presented in Fig. 17(b) is well reproduced by Eq. (1) as shown by the solid line. The frequency (the period) of this oscillation is 54 cm^{-1} (0.62 ps), which is nearly equal to that observed in the photoinduced *IN* transition (0.60 ps). Therefore, it can also be attributed to the lattice phonon corresponding to the dimeric molecular displacements. As shown in Fig. 26(b), the confined 1D *I* domain is produced immediately after the photoirradiation. Since each molecule in the 1D *I* domain has spin ($S=1/2$), the 1D *I* domain has the SP-like instability, although the size of *I* domain ($W_I \sim 5$) is not so large. We can consider that this instability will lead to the dimeric molecular displacements as shown in Fig. 26(c), which are detected as the coherent oscillation shown in Fig. 17(b).

The probe energy dependence of the amplitudes of this oscillation shown in Fig. 17(c) (the open circles) is quite similar to the differential reflectivity spectrum, $[R_I(4\text{ K}) - R_I(77\text{ K})]/R_N(90\text{ K})$, which corresponds to the increase of ρ by ~ 0.05 in the *I* phase. It supports the interpretation presented earlier. The important point to be emphasized is that the dynamical *NI* conversion [Fig. 26(b)] and the dynamical SP distortion [Fig. 26(c)] can be discriminated in the time domain. Other oscillatory structures with the period of ~ 50 ps seen in Fig. 16(b) are attributable to the shock wave discussed in Sec. VI B 1. In fact, the frequency of this oscillation is found to show probe-energy dependence characteristic of the shock wave.

C. Dynamical aspects of the photoinduced *IN* transition

In this subsection, we will discuss the physical picture of the photoinduced *IN* transition on the basis of the analyses presented in the previous subsections. For the resonant CT excitation in the *I* phase at 4 K, the confined 1D *N* domains composed of about 8 D^0A^0 pairs are initially photogenerated through the purely electronic processes, that is the first stage of the *IN* transition. In the *I* phase of TTF-CA, the *I* states are stabilized not only by the intrachain interactions but also by the interchain ones. The intrachain interactions are based upon the Madelung potential along the chain and the dimeric molecular displacements due to the SP mechanism. The interchain interactions are related with the Madelung potential along the direction perpendicular to the chain and the ferroelectric ordering of the dimeric molecular displacements.[13] Under these interchain interactions, a 1D *N* domain cannot spread over chain but is rather confined. The formation of the confined 1D *N* domains are followed by the coherent oscillations associated with the dissolution process of the molecular displacements. A number of the confined 1D *N* domains can make the neighboring *I* states unstable cooperatively. When the excitation density is larger than 0.3×10^{16} photons/cm^2, that is, 0.06 photon/*DA* pair, the *N* states are indeed multiplied at 4 K. In this stage, that is, the second stage of the *IN* transition, the multiplication occurs two-dimensionally within the absorption depth of the pump light (l_p), as seen in Fig. 20. It is quite reasonable, since the multiplication of the *N* states is a nonlinear process and occurs only when the amount of the initial 1D *N* domains reaches the critical density. Accordingly, in the region with $z > l_p$, the multiplication of the *N* states does not occur in this second stage up to $t_d \sim 20$ ps. The time scale (~ 20 ps) of this multiplication process is quite slow as compared with the time scale ($\ll 200$ fs) of the formation process of the confined 1D *N* domains. It is, therefore, natural to consider that the multiplication is not dominated by purely electronic process. A possible factor determining the time scale of the multiplication is the change of the unit cell volume or the lattice constants. As mentioned in the Sec. VI B 1, the volume of the unit cell is changed by 0.6% through the *NI* transition. Therefore, the multiplication of the *N* states should also be accompanied by the change of the lattice constants, which will proceed in the time scale of the acoustic phonons. This will be the reason for the fairly slow multiplication processes.

The period (~ 85 ps) of the slow coherent oscillation is about 4 times as large as the characteristic time of the multiplication process (~ 20 ps). Therefore, this coherent oscillation might also be related to the change of the volume or lattice constants in the semimacroscopic *N* state. Namely, the generation of the semimacroscopic *N* state induces the long-range deformation of the lattice due to the large lattice constants in the *N* state as compared with those in the *I* state and

then the change of the lattice deformation is coupled with the motion of the *NI* domain wall, that will result in the slow coherent oscillation.

After the multiplication process of the *N* states up to $t_d \sim 20$ ps in the second stage of the *IN* transition, another multiplication process occurs along the direction perpendicular to the sample surface up to $t_d \sim 40$ ps, that is the third stage of the *IN* transition. When the multiplication process in the second stage is completed, the semimacroscopic *N* state is produced near the sample surface. The *I* states near the interface of the *N* and *I* regions then become unstable due mainly to the lack of the interchain Coulomb attractive interactions. It is the reason why the multiplication along the *z* direction occurs. In this delayed multiplication process, the increase of the lattice constants should also be indispensable and then its time scale will be very slow ($t_d \sim 20-40$ ps).

When the temperature is raised to 77 K just below the *NI* transition temperature T_c, the efficiency of the photoinduced *I* to *N* transition is strongly enhanced due to the increase of the valence instability. At 77 K, the size of the confined 1D *N* domain ($\sim 24\ D^0A^0$) is three times as large as that ($\sim 8\ D^0A^0$) at 4 K and the multiplication of the confined 1D *N* domains occurs for very low excitation density (0.001 photon/*DA* pair). Nevertheless, the time of the multiplication process at 4 and 77 K is the same (~ 20 ps), as seen in Fig. 4. It indicates that the time scale of this process is not dominated by the instability of the electron-lattice system but by other origin such as the volume change as discussed here.

D. Difference of the dynamics between the photoinduced *IN* and *NI* transition

As discussed in the previous subsections, it is clear that there is a significant difference of the dynamical behaviors between the photoinduced *IN* and *NI* transitions. In the *IN* transition, the confined 1D *N* domains are multiplied through the cooperative interactions in the time scale of 20 ps, when the excitation density is high or the temperature is near T_c. In the *NI* transition, the confined 1D *I* domains are also generated just after the photoirradiation, but they decay up to $t_d \sim 20$ ps even for the high excitation density. Such a difference may be simply explained as follows. The ionic state of TTF-CA is the ferroelectric ordered state with the 3D ordering of dimeric displacements. Namely, the photoinduced formation of the *N* domain in the *I* phase corresponds to a dissolution process of the ordering, so that this process will be easily driven by photoirradiations. On the other hand, the *N* to *I* transition is a formation process of a 3D ordered *I* state. Considering this point, it is natural that the stable semimacroscopic *I* state is difficult to be produced by photoirradiations. Very recently, however, Collet *et al.* have reported from the time resolved x-ray study that the photoirradiation can stabilize the ferroelectrically ordered *I* state in the *N* phase.[10] The reason for the discrepancy between our results and theirs is not clear at present. It may be attributable to the difference of the excitation conditions, e.g., the pulse width and/or the photon density of the pump lights or the spot size of the pump lights relative to the sample size.

VII. SUMMARY

Dynamical aspects of the photoinduced phase transitions from ionic (*I*) to neutral (*N*) and neutral (*N*) to ionic (*I*) phases in organic CT compound, TTF-CA, have been investigated by the femtosecond pump-probe reflection spectroscopy. The transient reflectivity spectra of the intramolecular transition band of TTF sensitive to the change of the degree of CT have been measured as a function of the excitation density, temperature and excitation energy. To obtain quantitative information of the photoinduced transitions from the transient reflectivity spectra, we adopt the multilayer model. From the detailed analysis using this model, we have clarified the time characteristics of the amounts and spatial distributions of photoinduced products.

In the *IN* transition induced by the resonant excitation of the CT band, three processes are clearly demonstrated; (1) a confined 1D *N* domain, that is, a sequence of D^0A^0 pairs, is initially produced from a CT excitation, (2) the 1D *N* domains are multiplied through the cooperative interactions up to ~ 20 ps and semimacroscopic *N* states are stabilized within the absorption depth of the pump light, and then (3) the *IN* transition proceeds in the direction normal to the sample surface. The size of the confined 1D *N* domain initially generated and the efficiency of the multiplication process are strongly dependent on temperature. Near the *NI* transition temperature, the size is very large, exceeding 20 D^0A^0 pairs and the multiplication process is considerably enhanced. When the excitation energy is increased, the initial photoproducts are changed from the confined 1D *N* domains to the positively and negatively changed *N* domains. The size of the latter is considerably larger than that of the former, indicating the charge-carrier injection makes the neighboring *I* state strongly unstable.

The dynamics of the photoinduced *NI* transition has also been investigated in detail. The 1D *I* domain is initially produced by lights. Its size is, however, not so large even near the *NI* transition temperature, and the domains decay up to ~ 20 ps, even if the density of the *I* domains is increased. The results demonstrate that there is a clear difference of the dynamics between the photoinduced *NI* and *IN* transitions. Such a difference has been explained by considering the 3D ordering of the dimeric displacements (or equivalently the ferroelectric nature) in the *I* phase.

Other important results of this study were the observation of several kinds of coherent oscillations with subps or ps periods in the photoinduced reflectivity changes. In the photoinduced *IN* transition, the observed three kinds of oscillations with the period of ~ 0.6, ~ 50, and ~ 85 ps, are reasonably assigned to the dynamical dimeric displacements of molecules associated with the dissolution of the spin-Peierls distortions, the shock wave driven by the sudden volume change due to the photoinduced *IN* transition, and the oscillation of the *NI* domain boundary, respectively. In the photoinduced *NI* transition, the observed two kinds of oscillations with the period of ~ 0.6 and ~ 50 ps, are attributed to the dynamical dimeric displacements of molecules associated with the spin-Peierls instability and the shock wave, respectively. Note that the rapid oscillation with the period of ~ 0.6 ps reported here is the first example of the coherent

oscillation associated with the spin-Peierls instability and gives a direct evidence for the strong coupling between the charge (spin) and the lattice.

Finally, we would like to emphasize that the multilayer model adopted here is a powerful tool to analyze the results of pump-probe reflectivity spectroscopy, which is the most standard method to investigate photoinduced phase transitions of solids. Using this model, information about the time characteristics of not only amounts of the photoproducts but also their spatial distributions is provided.

ACKNOWLEDGMENT

This work was supported by a grant-in-aid from the Ministry of Education, Culture, Sports, Science and Technology of Japan.

[1] *Relaxations of Excited States and Photoinduced Structual Phase Transitions*, edited by K. Nasu (Springer-Verleg, Berlin, 1997).
[2] S. Koshihara, Y. Tokura, T. Mitani, G. Saito, and T. Koda, Phys. Rev. B **42**, 6853 (1990).
[3] S. Koshihara, Y. Tokura, K. Takeda, and T. Koda, Phys. Rev. Lett. **68**, 1148 (1992); Phys. Rev. B **52**, 6265 (1995).
[4] H. Matsuzaki, T. Matsuoka, H. Kishida, K. Takizawa, H. Miyasaka, K. Sugiura, M. Yamashita, and H. Okamoto, Phys. Rev. Lett. **90**, 046401 (2003).
[5] H. Matsuzaki, W. Fujita, K. Awaga, and H. Okamoto, Phys. Rev. Lett. **91**, 017403 (2003).
[6] S. Iwai, M. Ono, A. Maeda, H. Matsuzaki, H. Kishida, H. Okamoto, and Y. Tokura, Phys. Rev. Lett. **91**, 057401 (2003).
[7] S. Koshihara, Y. Takahashi, H. Sakai, Y. Tokura, and T. Luty, J. Phys. Chem. B **103**, 2592 (1999).
[8] T. Suzuki, T. Sakamaki, K. Tanimura, S. Koshihara, and Y. Tokura, Phys. Rev. B **60**, 6191 (1999).
[9] S. Iwai, S. Tanaka, K. Fujinuma, H. Kishida, H. Okamoto, and Y. Tokura, Phys. Rev. Lett. **88**, 057402 (2002).
[10] E. Collet, M. H. Cailleau, M. B. Cointe, H. Cailleau, M. Wulff, T. Luty, S. Koshihara, M. Meyer, L. Toupet, P. Rabiller, and S. Techert, Science **300**, 612 (2003).
[11] L. Guerin, E. Collet, M. H. Cailleau, M. B. Cointe, H. Cailleau, A. Plech, M. Wulff, S. Koshihara, and T. Luty, Chem. Phys. **299**, 163 (2004).
[12] J. J. Mayerle, J. B. Torrance, and J. I. Crowley, Acta Crystallogr., Sect. B: Struct. Crystallogr. Cryst. Chem. **35**, 2988 (1979).
[13] M. Le Cointe, M. H. Lemée-Cailleau, H. Cailleau, B. Toudic, L. Toupet, G. Heger, F. Moussa, P. Schweiss, K. H. Kraft, and N. Karl, Phys. Rev. B **51**, 3374 (1995).
[14] J. B. Torrance, J. E. Vazquez, J. J. Mayerle, and V. Y. Lee, Phys. Rev. Lett. **46**, 253 (1981).
[15] J. B. Torrance, A. Girlando, J. J. Mayerle, J. I. Crowley, V. Y. Lee, P. Batail, and S. J. LaPlaca, Phys. Rev. Lett. **47**, 1747 (1981).
[16] A. Girlando, F. Marzola, C. Pecile, and J. B. Torrance, J. Chem. Phys. **79**, 1075 (1983).
[17] Y. Tokura, Y. Kaneko, H. Okamoto, S. Tanuma, T. Koda, T. Mitani, and G. Saito, Mol. Cryst. Liq. Cryst. **125**, 71 (1985).
[18] Y. Tokura, T. Koda, T. Mitani, and G. Saito, Solid State Commun. **43**, 757 (1982).
[19] S. Horiuchi, Y. Okimoto, R. Kumai, and Y. Tokura, J. Phys. Soc. Jpn. **69**, 1302 (2000).
[20] J. B. Torrance, in *Low-Dimensional Conductors and Superconductors*, NATO ASI Series B155, edited by D. Jerome and L. G. Caron (Plenum Press, New York, 1987).
[21] Y. Kanai, M. Tani, S. Kagoshima, Y. Tokura, and T. Koda, Synth. Met. **10**, 157 (1984).
[22] S. Kagoshima, Y. Kanai, M. Tani, Y. Tokura, and T. Koda, Mol. Cryst. Liq. Cryst. **120**, 9 (1985).
[23] H. Okamoto, T. Koda, Y. Tokura, T. Mitani, and G. Saito, Phys. Rev. B **39**, 10 693 (1989).
[24] M. H. Lemée-Cailleau, M. Le Cointe, H. Cailleau, T. Luty, F. Moussa, J. Roos, D. Brinkmann, B. Toudic, C. Ayache, and N. Karl, Phys. Rev. Lett. **79**, 1690 (1997).
[25] S. Iwai, S. Tanaka, H. Kishida, H. Okamoto, and Y. Tokura, *Ultrafast Phenomena XIII*, Springer Series in Chemical Physics Vol. 71 (Springer, Berlin, 2003), p. 546.
[26] Y. Tokura, T. Koda, G. Saito, and T. Mitani, J. Phys. Soc. Jpn. **53**, 4445 (1984).
[27] C. S. Jacobson and J. B. Torrance, J. Chem. Phys. **78**, 112 (1983).
[28] Figure 5 was presented in the previous letter (Ref. 9), in which the scale of the horizontal axis was mistaken and should be doubled. Here, we report the correct figure.
[29] N. Nagaosa and J. Takimoto, J. Phys. Soc. Jpn. **55**, 2745 (1986).
[30] N. Nagaosa, J. Phys. Soc. Jpn. **55**, 2754 (1986).
[31] N. Nagaosa, J. Phys. Soc. Jpn. **55**, 3488 (1986).
[32] Y. Toyozawa, Solid State Commun. **84**, 255 (1992).
[33] T. Luty, H. Cailleau, S. Koshihara, E. Collet, M. Takesada, M. H. Lemée-Cailleau, M. Buron-Le Cointe, N. Nagaosa, Y. Tokura, E. Zienkiewicz, and B. Ouladdiaf, Europhys. Lett. **59**, 619 (2002).
[34] P. Huai, H. Zheng, and K. Nasu, J. Phys. Soc. Jpn. **69**, 1788 (2000).
[35] H. Okamoto, T. Mitani, Y. Tokura, S. Koshihara, T. Komatsu, Y. Iwasa, T. Koda, and G. Saito, Phys. Rev. B **43**, 8224 (1991).
[36] J. Y. Vinet, M. Combescot, and C. Tanguy, Solid State Commun. **51**, 171 (1984).
[37] A. Lietoila and J. F. Gibbons, Appl. Phys. Lett. **40**, 624 (1982).
[38] M. Nagai, R. Shimano, and M. Kuwata-Gonokami, Phys. Rev. Lett. **86**, 5795 (2001); M. Nagai and M. Kuwata-Gonokami, J. Lumin. **100**, 233 (2002).
[39] H. M. Ma, Y. X. Liu, Y. Fei, and F. M. Li, J. Appl. Phys. **65**, 5031 (1989).
[40] Y. Okimoto *et al.* (unpublished).
[41] A. Moreac, A. Girard, Y. Delugeard, and Y. Marqueton, J. Phys.: Condens. Matter **8**, 3553 (1996).
[42] A. M. Lindenberg, I. Kang, S. L. Johnson, T. Missalla, P. A. Heimann, Z. Chang, J. Larsson, P. H. Bucksbaum, H. C. Kapteyn, H. A. Padmore, R. W. Lee, J. S. Wark, and R. W. Falcone, Phys. Rev. Lett. **84**, 111 (2000).
[43] K. Tanimura and I. Akimoto, J. Lumin. **94–95**, 483 (2001).
[44] M. Fiebig, K. Miyano, Y. Tomioka, and Y. Tokura, Appl. Phys. B: Lasers Opt. **B71**, 211 (2000).